PAPER

Functional porous protein nanofibrils/polysaccharides aerogel beads for efficient dyes removal from water†

Mandana Dilamian,[a] Majid Montazer,[b] Hossein Yousefi,[cd] Daniel E. Otzen [iD][e] and Dina Morshedi [iD] *[a]

The rational design and fabrication of functional and feasible adsorbents with enhanced adsorption properties for pollutant removal remain challenging. Here, to achieve efficient adsorption of dyes, a radial-freezing technique was employed to develop freeze-dried bio-nanocomposites in the form of aerogel beads composed of cellulose nanofibers, protein nanofibers, and chitosan (CPCs). This strategy led to the formation of a spherical aerogel with a dandelion-like structure in the radial cross-section. FE-SEM micrographs of the aerogel beads revealed a highly porous morphology with a network of interconnected pores, allowing for the effective adsorption of liquids. The characterization results of the functional aerogel beads showed a remarkable ability to adsorb various cationic and anionic azo dyes. The maximum adsorption capacity of 1349.7 ± 34.36 mg g^{-1} and removal efficiency of nearly 100% in the initial 1000 mg L^{-1} Congo Red (CR) solution were obtained for CPCs aerogel beads. The resulting adsorption experimental data were fit by the sip isotherm and pseudo-second-order models. The porous structure of the CPCs aerogel bead enhanced the diffusion of dye molecules into the pores and inner surface. Furthermore, combined with the analysis results of FT-IR spectroscopy and XPS, multiple adsorption mechanisms (strong electrostatic interactions, hydrogen bonds, CH–π and π–π bonds) were ascribed between the CPCs composite and dye cations. It is believed that our CPCs aerogel beads can be regarded as a sustainable green bio-adsorbent for water remediation.

Introduction

Freshwater contamination caused by dyes is becoming a significant environmental problem. Dyes have extensive applications in various modern industries, including textiles, leather, food additives, paper printing, and cosmetics.[1,2] Due to their complex chemical structures, most dyes are biologically non-degradable and threaten aquatic ecosystems and human health.[3] The release of these intensely colored waste effluents without appropriate treatment also creates visual disturbances and hinders the penetration of light, thus impacting various biological processes within the watercourse. More than 60% of the annual production of dyes consists of azo dyes, which are soluble in water, exhibit high reactivity, and offer the most comprehensive range of colors.[4] Several water remediation approaches, including membrane separation,[5] photocatalytic degradation,[6] ion exchange,[7] electrochemical oxidation,[8] ozonation, coagulation,[4] and adsorption,[9,10] have been utilized to remove harmful dyes.[11–13]

Adsorption is an up-and-coming and straightforward technology for removing hazardous and detrimental contaminants from liquid waste, offering a high ratio of removal efficiency to cost.[14] In particular, porous materials such as aerogels are widely used absorbents for wastewater treatment.[14] Aerogels are solid materials with a highly interconnected porous structure. They are known for their exceptional properties such as extremely low density, high porosity, significantly high specific surface area, and excellent adsorption capacity.[15] The effectiveness of wastewater treatment processes is significantly influenced by the structural characteristics of aerogel composites, such as pore geometry (lamellar, dendritic, and cellular) and

[a] Bioprocess Engineering Department, Institute of Industrial and Environmental Biotechnology, National Institute of Genetic Engineering and Biotechnology (NIGEB), P.O. Box 14965/161, Tehran, Iran. E-mail: morshedi@nigeb.ac.ir

[b] Department of Textile Engineering, Amirkabir University of Technology (Tehran Polytechnic), 15875-4413, Tehran, Iran

[c] Laboratory of Renewable Nanomaterials, Department of Wood Engineering and Technology, Gorgan University of Agricultural Sciences and Natural Resources, 4913815739, Gorgan, Iran

[d] Nanonovin Polymer Co., Gorgan University of Agricultural Sciences and Natural Resources, 4913815482, Gorgan, Iran

[e] Interdisciplinary Nanoscience Centre (iNANO), Department of Molecular Biology and Genetics, Aarhus University, 8000 Aarhus C, Denmark

† Electronic supplementary information (ESI) available. See DOI: https://doi.org/10.1039/d4ma00380b

the type of structural framework (organic or inorganic).[16–19] The pore size and its fine distribution in porous aerogels are essential for flow dynamics, mechanical stability, and the ability to adsorb liquids or gases.[20] The potential use of ice-templating for developing porous aerogels with various pore morphologies has been reported in previous literature.[16] This is known as directional freezing or freeze-casting, which can provide a variety of pore morphologies with extensive potential to eliminate contaminants from water. The freezing direction refers to the nucleation and growth of ice crystals, which are highly dependent on the solidification rate. The freezing-direction technique is classified into four groups: non-directional, unidirectional, bidirectional, and radial freezing.[16,18] Integrating radial freezing with spraying can facilitate the development of colloidal particles with micro-porous 3D networks, providing a radial diffusion channel for mass transfer. In a recent study, Liao *et al.* prepared graphene oxide aerogel microspheres with dandelion-like structures through a radial-directional freezing–thawing process. The obtained aerogel microspheres with a highly porous and hydro-phobic structure revealed excellent absorptivity for oils and organic solvents (60–214 g g^{-1}).[21] In another report, graphene/chitosan composite aerogel microspheres with microchannel structures were developed *via* electrospraying and freeze-drying methods. The fabricated microspheres demonstrated a remarkable Young's modulus of 197 kPa. Results revealed that the oil adsorption kinetics of the microspheres followed the pseudo-second-order kinetic equation, while the isotherms aligned with the Langmuir model.[22]

Porous biocompatibility, cost-effectiveness, renewability, non-toxicity, and biodegradability of the bio-adsorbents have generated interest in using them in wastewater treatment. A variety of micro/nano-biopolymer-based aerogels have been designed and developed for the removal of contaminants from water.[23–26] Polysaccharides, including cellulose nanofibers (CNFs) and chitosan (Cs), are produced from abundant and cheap raw materials, offering promising alternatives in biomaterials. CNFs generally provide advantages such as exceptional strength, stiffness, safety, and the ability to tailor their surface chemistry, making them highly appropriate for fabricating structural materials such as aerogels.[27] Hence, cellulose-derived materials are more likely to be utilized as cost-effective adsorbents for removing contaminants such as heavy metals, pesticides, dyes, and nitroarenes in water/wastewater.[27–29] However, the limited functionality of CNFs hinders their effectiveness as a dye adsorbent. This can be improved by attaching functional moieties such as carbonyl, carboxyl, and amino groups to the surface of CNFs.[30] Cs demonstrates significant promise within sewage disposal due to its hydroxyl and amine functional groups, which exhibit a strong capacity for the adsorption of anionic organic pollutants.[22,31,32] However, pure Cs is limited by restricted surface area and inadequate mechanical properties. Incorporating Cs into CNFs matrix composite aerogels is a practical solution to enhance adsorption efficiency, improve stability, and increase surface area.[33] In this regard, various reports considered the preparation of hybrid aerogels made from Cs and CNFs using the freeze-casting method. For instance, Kim *et al.* reported that cellulose–chitosan foam exhibited a higher adsorption capacity (1170.2 mg g^{-1}) of CR compared to cellulose (623.2 mg g^{-1}).[34] In addition, Wang *et al.* prepared cellulose/chitosan porous aerogel to eliminate CR, for which the adsorption capacity of the dye reached 381.7 mg g^{-1} at pH 7.0.[35]

Incorporating functionalized active fillers such as whey protein fibrils into the composite materials can further enhance adsorption capacities.[36,37] Proteins with an abundance of amino and carboxyl groups can actively participate in the adsorption process.[38,39] Proteins can form polyelectrolyte complex (PEC) hydrogels with chitosan, eliminating the requirement for additional auxiliaries.[40] For instance, Tan *et al.* fabricated the chitosan-quinoa bran aerogel using the ice-templated assembly method that efficiently adsorbed CR and Cu^{2+} with a maximum adsorption capacity of 182.48 and 96.25 mg g^{-1}, respectively.[41] In this study quinoa bran was used as the by-product of quinoa processing, which was directly mixed with the chitosan–acetic acid solution.

Under appropriate denaturation and hydrolysis conditions, whey protein, a by-product generated from the cheese-making process, can undergo self-assembly to form protein nanofibrils (PNFs).[38,42–44] The environmentally friendly characteristics of the process contribute to developing a cost-efficient technology with a minimal ecological footprint. PNFs are bundles of elongated supramolecular filaments that exhibit a well-organized structure, primarily stabilized by β-sheet secondary structures. The structure of PNFs (several μm lengths and ∼10 nm width) provides an exceptionally high surface-to-volume ratio, ensuring that most amino acids are exposed on the surface.[45] Consequently, PNFs exhibit exceptional efficacy in removing heavy metals, dyes, and radioactive pollutants.[46–48] Notably, the flexible structure of PNFs promotes the formation of entangled networks even at low concentrations, making them exceptionally suitable for developing low-density and three-dimensional porous aerogels.[43] Nonetheless, PNFs-based adsorbents suffer from weak mechanical properties.[49–53] Hence, it is imperative to investigate effective modification techniques to enhance the characteristics of PNFs aerogel. We need to enhance the structural integrity of fibrillar networks of functional protein fibrils while maintaining functional surfaces.

In this study, we focused on creating a ternary bead composite using CNFs, Cs, and PNFs through the radial freeze-casting technique. Our work emphasizes the importance of integrating functional biomaterials (PNFs and Cs) into the fibrous structure of CNF. We used a simple chemical process with a homogenizer to prepare a Cs hydrogel with a neutral pH. Additionally, we formed spherical aerogels to increase the surface area and achieve the best adsorption efficiency.

We examined the impact of the CNFs/Cs/PNFs aerogel beads composite (CPCs) on the adsorption capabilities of various dyes. Specifically, we investigated the adsorption efficiency of CR, a commonly used azo dye, by analyzing dosage, dye concentrations, contact time, pH value, adsorption time, and

initial concentrations. We measured CR adsorption isotherms and removal kinetics in the presence of CPCs aerogel beads. Meanwhile, the physical and chemical characteristics of the CPCs, including surface morphology, pore distribution, surface area, chemical composition, crystalline phase, and zero-charge point, were evaluated and analyzed. Finally, the adsorption mechanism was analyzed by using field emission scanning electron microscopy- energy dispersive X-ray spectroscopy (FE-SEM-EDX), Fourier transform infrared spectroscopy (FTIR), and X-ray photoelectron spectroscopy (XPS).

Experimental

Materials

Whey protein isolate (WPI) was provided by a dairy company, (Iran). Cellulose nanofibers with 3 wt% solid mass were mechanically prepared from wood pulp in Nanonovin Polymer Co. (Iran) (Fig. 1A). The polyamide-amine-epichlorohydrin (PAE) resin (20 wt%) as a wet strength agent for crosslinking was kindly provided from Solenis (Kymene GHP20, Solenis Denmark ApS). Chitosan (M_w: 100 000–300 000 g mol^{-1}, DD >85%) was purchased from Sigma-Aldrich Acros-Organics. Citric acid (CAS Number 77-92-9) was obtained from Sigma-Aldrich. Thioflavin-T (CAS Number 2390–54-7), Crystal Violet (CV, CAS Number 548-62-9, C.I. 42555), malachite Green (MG, CAS Number 569-64-2, C.I. 42000), Bismarck Brown-R (BB, 40%, CAS Number 5421–66-9, C.I. 21010), chrysoidine-G (CG, dye content: 90%, CAS Number 532–82-1, C.I. 11270), acid red-88 (AR, 75%, CAS Number 1658–56-6, C.I. 16250), reactive black-5 (RB, 50%, CAS Number 17095-24-8, C.I. 20505), Congo Red (CR, ≥37%, CAS Number 573–58-0, C.I. 22120), direct violet-51

(DV, 50%, CAS number 5489–77-0, C.I. 42520), and reactive orange-16 (RO, ≥70%, CAS Number 12225-83-1, CI 21260), sodium hydroxide (NaOH), acetic acid (CH$_3$COOH), and hydrochloric acid (HCl, 37%w/v) were from Merck (Germany). All solutions were prepared using deionized water.

Preparation of chitosan hydrogel

Fig. 1B illustrates the procedure for preparing Cs beads. Initially, Cs powder (3% w/v) was dissolved in acetic acid (1% v/v) and stirred overnight to ensure complete dissolution. To create spherical Cs beads, the viscous chitosan–acetic acid solution was added drop-wise through a needle into a 200 mL bath containing NaOH 4M. The distance between the needle and the surface of the NaOH solution was 5 cm. This process consisted of two primary stages. First, droplets of the initial solution were dispersed and then underwent gelation when they encountered the liquid containing the cross-linking agent. Gelation occurred as sodium hydroxide diffused into the droplets, resulting in the formation of polymer cross-links. Thus, gel particles with a spherical shape were generated. These gel particles were subsequently filtered and rinsed with deionized water to eliminate any remaining alkalinity and form neutral Cs beads. Afterward, the resulting beads were added to 100 mL deionized water, and the dispersion was mixed vigorously using a mechanical mixer (Bead-Beater; Hamilton Beach Commercial) for 15 min to ensure homogenous hydrogel particles throughout the suspension. The weight fraction of the Cs hydrogel suspension was determined using gravimetric analysis.

β-Lactoglobulin monomer purification

β-Lactoglobulin (βLG) monomers were purified from WPI according to the Usuelliet *et al.* protocol.[53] Briefly, 10 g of
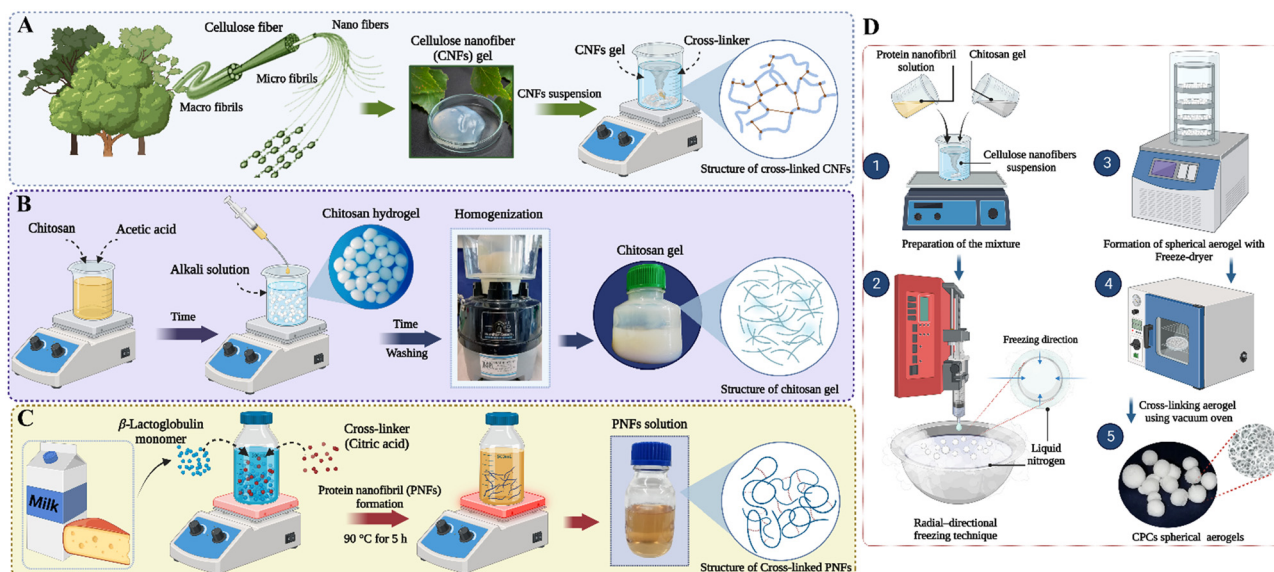

Fig. 1 Schematic illustration of fabricating composite aerogel beads. The preparation process of: (A) CNFs suspension, (B) chitosan hydrogel, and (C) protein nanofibrils from βLG monomers. (D) The schematic processes of producing the CPCs aerogels: The dispersion of CNF, PNF, and Cs at a ratio of 1:1.25:1.25 (CNFs:PNFs:Cs) were prepared with agitating for 15 min.[1] Next, the dispersion was frozen through the radial-directional freezing technique.[2] Afterwards, the frozen aerogel beads were freeze-dried to obtain CPCs aerogel beads.[3] The CPCs aerogel beads were dry-crosslinked in a vacuum oven (120 °C for 3 h).[4,5]

WPI was dissolved in 90 g of Milli-Q water, and the pH was adjusted to 4.2 with HCl. Subsequently, the WPI solution was incubated in a shaking bath at 60 °C for 3 h. During this process, the WPI solution became cloudy as a sign of α-lactalbumin agglomeration. The turbid solution was then transferred to plastic Falcon tubes and centrifuged at 12 000 r for 20 minutes to separate the α-lactalbumin fraction. The resulting solution was transferred into a Schott bottle.

Preparation of protein nanofibrils

The fibrillation of βLG (Fig. 1C) was followed according to the previously described procedures.[49,54] Initially, the βLG monomer was dispersed in Milli-Q water at a concentration of 2 wt%. The pH of the solution was then lowered to pH 2 using HCl 2M. The βLG solution was incubated at 90 °C for 5 h, during which the protein solution underwent magnetic stirring at 150 rpm (PNFs). Subsequently, the protein solution was quenched in mixtures of ice and water to stop fibrillation. To enhance the interactions between protein fibrils, PNF-C1 and PNF-C1.5 samples were prepared by incorporating CA at 1 and 1.5wt% into the βLG dispersions. The same procedure was employed for their preparation. The as-prepared fibril solutions were kept at 4 °C for future usage. Notably, the βLG monomer underwent unfolding, hydrolysis, and self-assembly throughout the incubation process, ultimately forming PNFs.[55] CA acts as a cross-linking agent in protein fibril formation. This contains carboxyl groups that can form covalent bonds with amino groups in the amyloidogenic proteins. These crosslinking interactions can stabilize the protein aggregates and promote the formation of PNFs.

Fabrication of cellulose nanofibers/chitosan/protein nanofibrils aerogel beads

The schematic production of the CPCs aerogels is shown in Fig. 1D. Initially, a certain amount of CNFs suspension was dispersed in deionized water and stirred for 10 min at 300 rpm in an ice bath. Next, a weighed amount of PAE as a cross-linking agent (CNFs to the cross-linker ratio of 10 : 1) was injected drop-wise into the CNFs dispersion. Then, the mixture was sonicated with an ultrasonic bath (at 250 Watt) for 10 min. In our previous study, the optimum component ratio for preparing CPCs composite aerogels was determined.[56] We discovered that the best ratio of components, specifically 1 : 1.25 : 1.25 (CNFs : PNFs : Cs), exhibited exceptional mechanical stress resistance in wet conditions. Furthermore, this optimal ratio not only showcased excellent performance in wet conditions but also led to the creation of a cylindrical composite aerogel. Herein, the resultant CNFs/PAE dispersion was progressively mixed with an equal amount of PNFs and Cs solutions (1.6 wt%) at a ratio of 1 : 1.25 : 1.25 (CNFs : PNFs : Cs), and the mixture was stirred for 15 minutes in an ice bath (Fig. 1D-1). Afterward, the mixture was frozen *via* radial-directional freezing technique using liquid nitrogen (Fig. 1D-2) and further lyophilized in a freeze-dryer (Christ Freeze Dryer, Alpha 1–2 LD plus) at −80 °C for 24 h to obtain CPCs aerogel beads (Fig. 1D-3). Finally, the spherical aerogel beads were dry-crosslinked in a vacuum oven at 120 °C

for 3 h to ensure covalent cross-linking (Fig. 1D-4,5). The CNFs and CNFs/Cs (CCs) aerogel beads were also formed as control samples following a similar protocol. The cross-linked pure CNFs aerogel beads were prepared from the aqueous solution of CNFs/PAE (1.6 wt%, 10 : 1). CCs aerogel beads were formed from the uniform mixture of CNFs and Cs suspensions (1.6 wt%) at a mass ratio of 3 : 7.

Material characterization

Thioflavin T fluorescence assay. To monitor the progress of fibril formation, 10 μL aliquots of protein solutions (namely, PNFs, PNF-C1, and PNF-C1.5) were collected at the end of the fibrillation process and diluted with 490 μM of 12 μM thioflavin T (ThT) solution in 10 mM Tris buffer 10 mM (pH 8).[36,57] ThT fluorescence intensity of different samples was measured in the range of 450 to 550 nm using a Varian Cary Eclipse fluorescence spectrophotometer with excitation at 440 nm (slit-width of 5 nm) and measuring emission intensity at 480 nm (slit-width of 5 nm). All measurements were performed in triplicate.

Analysis of structure and morphology of the aerogels. The morphological features and surface characteristics of freeze-dried CNFs, Cs, PNFs, and composite aerogel (CPCs) were observed with a field emission scanning electron microscope (FE-SEM) (MIRA3, TESCAN) with an acceleration voltage of 15 kV. The composition of elements on CPC aerogel beads before and after CR adsorption was recorded using an energy-dispersive X-ray spectroscopy (EDX) on the FE-SEM. The sample was scanned at 1500 magnification with a 15 kV accelerating voltage.

Specific surface area and pore size distribution. Nitrogen adsorption–desorption isotherms of CPCs aerogel beads were determined from an ASAP 2020 instrument (Micrometrics, USA) at 77 K. The determination of Brunauer–Emmett–Teller (BET) analysis followed a multipoint BET method,[58] using a relative vapor pressure (P/P_0) range of 0.05–0.20 at −196 °C. The pore size distribution was obtained from the N_2 adsorption branch of the isotherm, employing the Barrett–Joyner–Halenda (BJH) method. Total pore volume measurement was based on the amount adsorbed at a relative pressure of $P/P_0 = 0.98$.

Fourier transform infrared spectroscopy (FTIR)

The chemical structure and functional groups of the freeze-dried PNFs, CNFs, Cs, and composite aerogel beads were investigated by FTIR (Bruker Tensor 27 spectrometer, Karlsruhe) in the range of 4000 to 400 cm^{-1}. Each dry sample was grounded, blended with KBr (1 : 100, w/w), and then pressed to prepare transparent pellets.

Wide-angle X-ray diffraction (XRD)

The XRD patterns of the freeze-dried PNFs, CNFs, Cs, and composite aerogel beads were recorded using an X-ray diffractometer (Equinox 3000 INEL) equipped with CuK$_\alpha$ ($\lambda = $ 1.54056 nm) radiation (operating at 40 kV and 40 mA). Measurements were performed in the 2θ range 5–40° with a step size of 0.026° at 25 °C.

Zeta potential

The surface area and the surface charges of the composite aerogel beads (CPCs) were calculated using zeta potential (Malvern, UK) at 25 °C. The dry CPCs aerogel beads (15 mg) were added into 20 mL of deionized water and the pH of the suspension was adjusted with NaOH 0.1 N and hydrochloric acid to 7.4. After 24 h, the supernatant was collected for zeta potential measurements.

X-ray photon spectroscopy (XPS)

A high-resolution X-ray photoelectron spectrometer (UIVAC-PHI) (XPS, Bes Tek instrument, Germany) was utilized to record the surface composition of CPCs aerogel for C 1s, N 1s, S 2p, and O 1s elements. The instrument was equipped with an Al-Kα source (1486.6 eV, 45 W), and the CPCs aerogel beads were conditioned and investigated at 10^{-10} mbar. The XPS data were analyzed using CasaXPS v2.3.2PR1.0 software.

Adsorption experiments

The developed aerogel composite beads (0.0025–0.075 mg) were added to 25 mL^{-1} of dye solution (50–2000 mg L^{-1}), while the pH medium was adjusted in the range of 4–10 using NaOH 0.1 M and HCl. The mixture of adsorbent and dye was agitated using a rotator shaker at a speed of 100 rpm and a temperature of 28 °C. At specific time intervals (1–180 min), the residual dye concentration was estimated using an EPOCH12 plate reader (BioTek, Winooski, Vermont, USA) at their maximum absorbance wavelength (λ_{Max}: at 497 nm for CR, 590 nm for CV, 620 nm for MG, 580 nm for BB, 470 nm for Chr, 500 nm for AR, 590 nm for DV, 554 nm for RB, and 493 nm for RO). The dye adsorption capacity at equilibrium (q_e, mg g^{-1}, eqn (1)) and the removal efficiency (η, %, eqn (2)) onto aerogel beads were calculated according to the following equations:

$$q_t = \frac{(c_0 - c_t)V}{m} \qquad (1)$$

$$\eta(\%) = \frac{(c_0 - c_t)}{c_0} \times 100\% \qquad (2)$$

where C_0 (mg L^{-1}) and C_t (mg L^{-1}) are the initial and equilibrium concentration of dye at the time (t) in minutes, respectively; and V (L) is the volume of the dye solution, and m (g) is the dosage of adsorbent. All measurements were performed in triplicate.

Results and discussion

Preparation of spherical composite aerogel

Tunable physicochemical properties, such as porosity, pore size, surface area, surface roughness, permeability, and function ability, directly influence the performance of an adsorbent to remove various contaminants efficiently. Hydrophilic composite sorbents, such as Cs and CNF-based aerogels, demonstrate strong molecular interactions with water, enabling efficient molecular transport in wastewater treatment processes. Furthermore, the polysaccharide polymer chains

contain a large number of hydroxyl and amine groups, which enables them to be easily modified for various applications. Incorporating functional PNFs within the surface pores of polysaccharide-based aerogels enhances accessibility and affinity toward the targeted pollutants,[20,53] further suggesting that the functional PNFs can be blended with polycationic moieties such as Cs to form polyelectrolyte complexed hydrogels.[40] In this study, porous cross-linked CNFs aerogel beads with the ability to support functional biopolymers such as Cs and PNFs were developed. The covalent cross-linking between native nanofibrils and cross-linkers (PAE) led to a cross-linked fibrous CNFs aerogel with high stability in aqueous solution.[17,26]

The schematic diagram in Fig. 1A–D shows the preparation procedure of the functional composite spherical aerogel using an ice-templating technique (Fig. 1D) from as-prepared precursors, namely, a natural CNFs suspension (Fig. 1A), a Cs hydrogel (Fig. 1B), and a PNFs solution (Fig. 1D). In the hydrogel state (Fig. 1B), Cs polymeric chains are physically interconnected by interactions such as hydrogen bonding and electrostatic attractions, which are the dominant interactions for forming the 3D network of Cs beads. In fact, at low pH (diluted acidic solution), Cs is positively charged, and through neutralizing the cationic amine sites (–NH$_3^+$) are deprotonated to –NH$_2$, resulting in a significant reduction in ionic repulsion within polymer chains, enabling the emergence of hydrogen bonding between polymeric chains.[40] The PNFs of βLG are semi-flexible colloids obtained from the protein aggregates. At specific fibril concentrations, these fibrils are self-assembled and create physical hydrogels. However, the elastic moduli of PNFs gels are often low (10–50 Pa), resulting in a weak fibril network[59] that restricts further applications. One approach to boost the strength and mechanical properties of PNFs gels is using low molecular weight ions to form an ionic cross-linked matrix. Nyström *et al.* prepared the first cross-linked PNFs aerogel with high water stability only by adding butane tetra-carboxylic acid to the fibril dispersion. However, in this investigation, citric acid (CA, cheap non-toxic polycarboxylic acid) was added to the protein solution to strengthen the PNFs network (Fig. 1C). As a hypothesis, CA is assumed to be uniformly distributed within the PNFs gel network, enhancing the electrostatic interaction between the amino group of the PNFs polymeric chain and the carboxylic group of citrate, resulting in a cross-linked PNFs gel (Fig. 1C). This hypothesis was further validated using analytical approaches (Fig. S1A and B, ESI†).

FE-SEM analysis

The surface morphological features of pristine CNFs, Cs, and PNFs, as well as an aerogel bead composite (CPCs), were investigated by FE-SEM. The CNFs aerogel bead with a concentration of 1.6 wt% (Fig. S2A, ESI†) exhibited a porous structure with a wide range of pore sizes classified into small and large pores (Fig. S2B–D, ESI†). The tiny pores were formed due to nanofiber network entanglement in cellulose platelets, whereas the large pores were those created as a result of ice crystal sublimation during the freeze-drying.[17] The surface

morphology of the freeze-dried Cs gel, on the other hand, revealed an uneven porous structure (Fig. S2E, ESI†). The crack in Fig. S2F (ESI†) resulted from the growth of ice lamella within the Cs gel and the formation of interstitial space between accumulated Cs during the freeze-drying. However, high-magnification FE-SEM images (Fig. S2G and H, ESI†) revealed the high porosity and the fibrillar interconnected structure of freeze-dried Cs gel. These features are highly beneficial for developing a bio-based composite aerogel. The surface morphology analysis of pristine PNFs derived from βLG indicated smooth, compact layered sheets (Fig. S2I and J, ESI†). The surface of PNFs contained multiple cracks extending several micrometers, as illustrated in Fig. S2J and K (ESI†). However, high magnification FE-SEM micrographs (Fig. S2L, ESI†) revealed smooth, homogeneous, and paper-like accumulating layers of the PNFs.

To obtain a porous aerogel with superior pore geometry and rational pore size distribution for waste-water applications, two distinct freezing mechanisms of unidirectional freeze-casting and radial freezing were employed. In unidirectional freeze-casting, the CPCs dispersion was cast into a cylindrical mold placed directly with liquid nitrogen from the bottom for a defined period. The ice nucleated and grew unidirectionally from the bottom to the top of the mold along the imposed thermal gradient. Subsequently, the ice crystals were sublimated using a freeze-drying process and formed a 3D monolith aerogel (Fig. 2A).

Unlike unidirectional freezing, radial freezing consists of two steps: spraying and ice-templating.[19,60] In radial freezing, the CPCs dispersion was dropped into liquid nitrogen via an electric nozzle tube. Ice crystals immediately started to nucleate and grow from the surface of droplets into the interior along radial directions. Finally, the frozen spherical samples were freeze-dried to sublimate the ice crystals inside the structure and translated to porous aerogels in 3D spherical shapes (Fig. 2E).
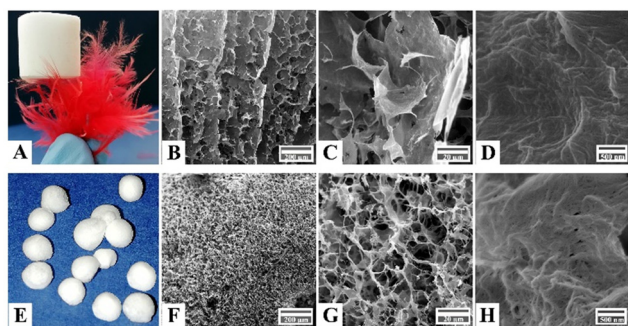
Fig. 2A shows an ultra-light cylindrical composite aerogel (supported by a dandelion) generated by an initial gel with a concentration of 1.6 wt%. FE-SEM images in Fig. 2B and C revealed a hierarchical porous structure of the cylindrical composite aerogel prepared by the unidirectional freezing technique. The lamellar walls observed in Fig. 2B resulted from the pushing forces applied by the growing ice crystals, which constrained the solid polymers into the space between the ice.[17,60] Specifically, fractions of the solid polymer were trapped in ice crystals, causing the formation of inter-layer bridges formation between the lamellar walls (Fig. 2C). While the cylindrical composite aerogel was macro-porous, mesoporous structures (diameters between 2 and 50 nm) were difficult to detect on the walls of aerogel at higher magnification (Fig. 2D).

The technique of radial-freezing successfully created an open porous aerogel with uniform pore size distribution (Fig. 2F–H). Unlike the cylindrical composite aerogel (Fig. 2B), the surface morphology of CPCs spherical aerogel displayed a hierarchical porous structure with cellular interconnected pores (Fig. 2G). Interestingly, the composite spherical aerogel presented superior pore geometry, in which the interlinked pores provide pathways for rapid diffusion of fluids from the surface to the interior fractions (Fig. 2G). Considerably, fine-scaled pores were observed inside the thin walls of the channel (Fig. 2H). As shown in Fig. 2H, these pores facilitate superior mass transport and uniform fluid dispersion inside the porous structure. As a result, the radial freezing approach was chosen for creating spherical composite aerogels due to the enhanced pore morphology, as well as the simplicity, accessibility, and reproducibility of the process.[16,19,61]

The CPCs aerogel beads had a well-preserved spherical shape that can sit firmly on top of a feather without disrupting its barbs (Fig. 3A). The surface (left) and the cross-section (right) of a perfectly spherical aerogel prepared through a radial-directional freezing mechanism are depicted in Fig. 3B. The inner structure of the CPCs aerogel sphere revealed a radial-patterned-like shape, indicating that the CPCs spherical droplets uniformly cooled from the surface to the interior; hence, the ice crystals nucleate and grow along the radial directions and form dandelion-like structure (Fig. 3C).[19,21,62] The FE-SEM image of the lyophilized spherical aerogel revealed a radial-center-diverging microchannel structure (Fig. 3D) and a highly porous morphology.[63] Fig. 3E shows the external surface of the porous CPCs aerogel bead, which had an average diameter of 2.2 mm. The surface morphology of the CPCs aerogel (Fig. 3F) revealed a network of interconnected pores with ultra-thin and uniform film-like walls of assembled composite. Smaller pores were also observed in Fig. 3G and H. The obtained aerogel bead exhibited a dandelion-like structure in the radial cross-section (Fig. 3J), in which the channels/pores of the aerogel were radially aligned using a radial freezing technique. The pore channels of CPCs aerogel are essential factors affecting the structure and physicochemical properties of the CPCs aerogel.

These cellular interconnected pore channels of CPCs aerogel provide abundant transport pathways between multiple porous
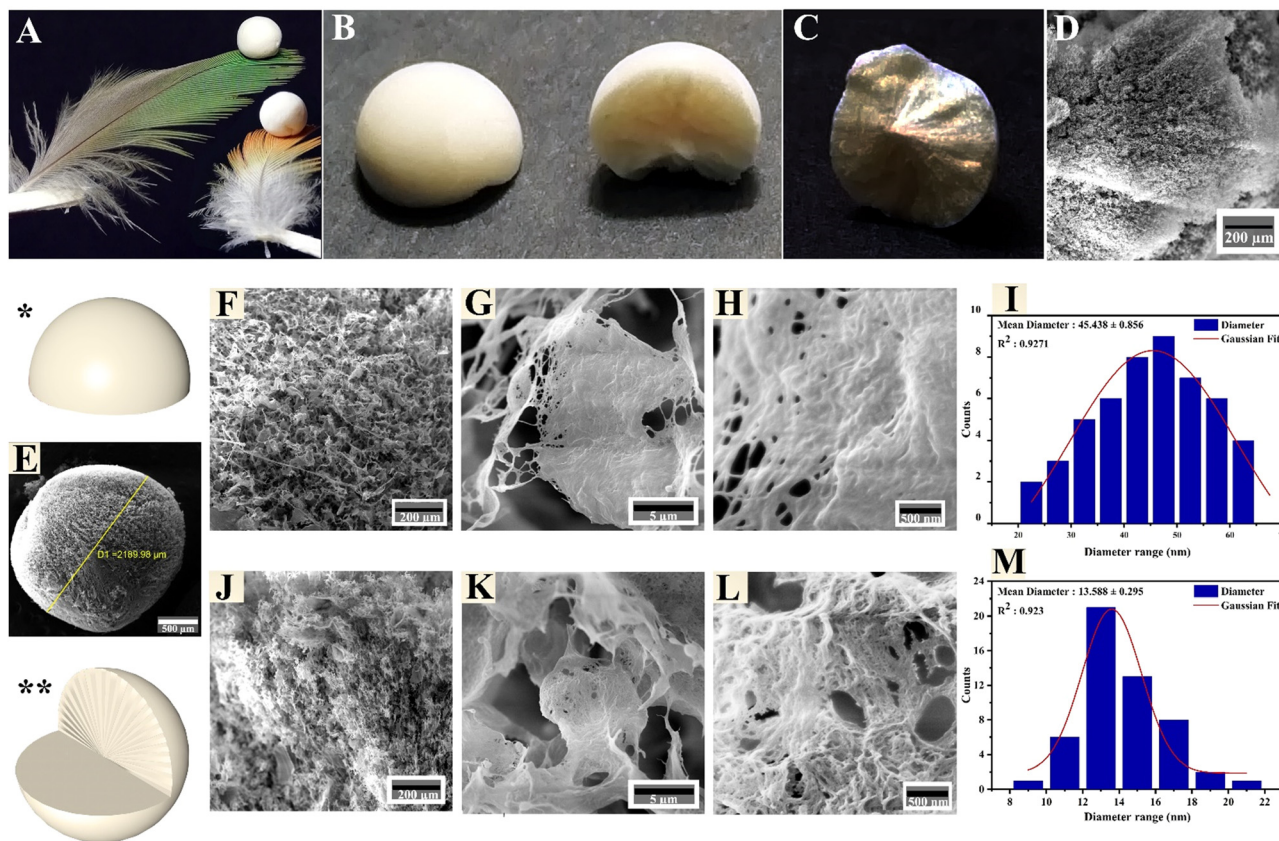

Fig. 2 Comparing two distinct freeze-casting techniques: (A) the digital photo of cylindrical CPCs aerogel prepared through unidirectional freezing technique, standing on top of a feather. (B) FE-SEM image, (C) and (D) high-resolution FE-SEM images of the cylindrical composite aerogel. (E) Digital photo of highly porous CPCs aerogel beads prepared by radial-freezing technique. (F) FE-SEM image, (G) and (H) high-resolution FESEM images of the CPCs aerogel bead.

Fig. 3 Assessing the topology of the fabricated beads. (A) Photo of CPCs aerogel beads, representing the CPCs aerogel sitting on top of a feather. (B) Surface (left) and cross-section (right) of a perfectly spherical CPCs aerogel. (C) Inner structure of the CPCs aerogel sphere illustrating a radial-patterned-like shape. (D) FESEM image of the spherical aerogel revealing a center-diverging microchannel structure. (E) FE-SEM images of CPCs aerogel bead, (Morphology evaluations from the *surface and ** cross sections of the aerogel bead). (F) Network of interconnected pores on the surface of CPCs aerogel, (G) and, (H) high-resolution FE-SEM images from the surface of aerogel. (I) Fiber diameter distribution extracted from the FE-SEM images (G) and (H). (J) Cross-section of the CPCs aerogel with dandelion-like structure, (K) and, (L) high-resolution FE-SEM images from the cross-section of aerogel bead, (M) Fiber diameter distribution extracted from the FE-SEM images (K) and (L).

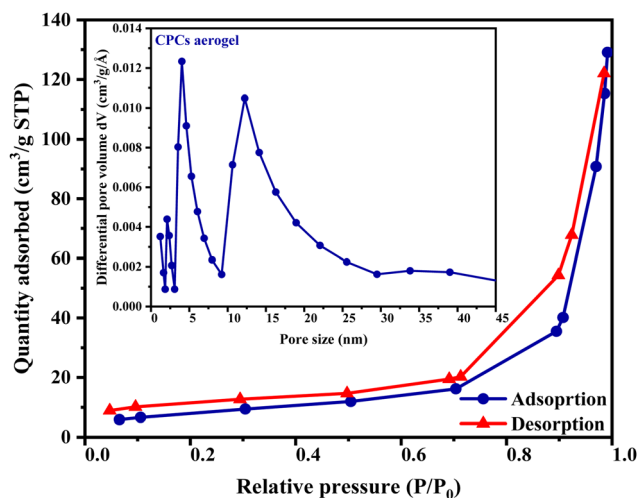layers, capable of taking up, separating and removing dye molecules which can furthermore interact with functional groups ($-COOH$, $-OH$, and $-NH_2$) within the pore channels. As shown in Fig. 3K, the thin layers of open cells in the aerogel contained a multitude of pores, creating a highly porous structure that allows for effective diffusion and adsorption of liquids. Additionally, the interconnected network of pores contributes to the mechanical stability of the aerogel, preventing collapse or deformation. High magnification FE-SEM images of CPCs aerogel in Fig. 3H and L revealed that the porous platelets of the aerogel were composed of interconnected fibrils with different size distributions. According to the statistics obtained from Digimizer software, the individual fibrils on the surface of the CPCs composite aerogel had a mean diameter of ~ 45 nm (Fig. 3I), while fibrils with a mean diameter of ~ 14 nm were observed within the interior walls of the porous aerogel (Fig. 3M).

Specific surface and pore structure of CPC

Brunauer–Emmett–Teller (BET) analysis was used to investigate the surface area of as-prepared aerogel beads. The results shown in Fig. 4, demonstrated accurate information about the specific surface area and porosity characteristic (pore volume and pore size) of CPCs aerogel. According to the

Fig. 4 Surface and pore characteristics of CPCs aerogel: N_2 adsorption/desorption isotherms (inset shows the pore size distribution for CPCs aerogel).

isotherm classification proposed by IUPAC,[64] the BET isotherm of CPCs aerogel revealed a typical class IV hysteresis loop with a sharp capillary condensation step at a relative pressure (P/P_0) of 0.5–1, indicating the presence of mesopores and macropores of aerogel beads.[65] Based on the nitrogen adsorption–desorption isotherms, the calculated specific surface area and the total pore volume were 29.61 m^2 g^{-1} and 0.2 cm^3 g^{-1}, respectively. The Barrett–Joyner–Halender (BJH) pore-size distribution curve of CPCs aerogel in the inset to Fig. 4 showed a bimodal distribution with a sharp peak at 5 nm followed by a broader peak centered at 12 nm, demonstrating that the CPCs aerogel beads were mostly mesoporous.[64] Expectedly, the results of BET were consistent with the high-resolution FE-SEM observations, implying that the CPCs aerogel has a porous structure consisting of mesoporous and flexible thin walls, which could endow the CPCs aerogel with enhanced adsorption capacity and rapid mass transportation of liquid.

Chemical structure analysis

FTIR analysis. The functional groups of various aerogel beads, namely, CNFs, CCs, PNFs, and CPCs composite aerogel, were shown in Fig. 5A. Overall, the FTIR spectrum of all samples exhibited a broad band at approximately 3400 cm^{-1} attributed to the stretching of hydroxyl (–OH) groups overlapped with amine (–NH$_2$) groups. Bands with similar intensities around 2900 cm^{-1} and 2870 cm^{-1} are ascribed to the stretching vibration of both asymmetric and symmetric C–H groups. The spectrum of pure PNFs (the image in Fig. S3, ESI†) revealed a characteristic sharp band at 1639 cm^{-1} due to the C=O backbone stretching vibrations of the amide I group of polypeptide chains. In addition, the bands at 1540 cm^{-1} and 1217 cm^{-1} are associated with a combination of C–N stretching and N–H in-plane bending (amid II) and amid III regions in protein, respectively.[12,43,54] The wide amide band at 3286 cm^{-1} (N–H stretching) represented the strength of intermolecular

hydrogen bonding in PNFs.[66] No specific band attributed to a backbone C–C stretching vibration in the 850–960 cm^{-1} range was detected. In conjunction with the absorption peak of the amide II region, this result indicated that the protein might have the structure of random-coil.[66] Upon cross-linking with CA (Fig. S3 and Fig. 5A, PNF-C1, ESI†), a new intense peak arose at 1720 cm^{-1}, attributing to the carbonyl ester groups, resulting from chemical cross-linking interactions within the –COO$^-$ group of CA and –N–H group of PNFs.[3] The amide I and amid II peak positions remained unchanged for cross-linked protein fibrils (PNFs-C), while the peak intensities were moderately reduced. After cross-linking, the peak position of the amide III at 1235 cm^{-1} shifted to a lower wavelength (1217 cm^{-1}) and merged with the C–C and C–O stretching vibrations peaks in CA. These findings confirm the occurrence of the cross-linking between PNFs and are consistent with previous results that investigated the FTIR spectra of amyloid fibrils after cross-linking with 1,2,3,4 butanetetracarboxylic acid (BTCA).[59,67] The spectrum of CNFs aerogel beads exhibited a strong peak in the 898–1160 cm^{-1} region, referred to as C–O stretching in the glycoside linkage,[17,68] which represents the prominent feature peak of polysaccharides (Fig. 5A, CNFs). Notably, the detected peaks at 1640 cm^{-1} (carbonyl group of amide I) and 1550 cm^{-1} (N–H bending of amide II) confirmed the presence of PAE as a crosslinker and suggested the formation of self-crosslinking through its epichlorohydrin groups and the external covalent crosslinking between CNFs chains after heat treatment.[17]

The characteristic peaks of CCs aerogel beads (Fig. 5A, CCs) were entirely similar to that of the CNFs (Fig. 1B), even though the peaks at 3367 cm^{-1} and 1060 cm^{-1} became sharper.[69,70] Moreover, the adsorption peaks of carbonyl (amide I) and N–H groups in Cs merged with the functional groups of the bonded PAE, and thus, a broader peak in the 1520–1690 cm^{-1} range appeared. These results also indicated that the CCs aerobead structure was effectively crosslinked *via* intermolecular interactions between CNFs, PAE, and Cs. Compared with CNFs, CCs, and PNFs-C1 aerogel beads, the FTIR spectrum of CPCs composite aerogel revealed the functional groups of its original components (Fig. 5A, CPCs). However, the characteristic bands of Cs and PNFs-C1 were merged with that of the CNFs (the major component of the composite aerogel), making them challenging to recognize individually. Nevertheless, after the incorporation of PNFs into the CCs hybrid composite, the peak intensities of amide I (1645 cm^{-1}) and amide II (1546 cm^{-1}) increased significantly, suggesting an interaction of PNFs with the CNFs and Cs in CPCs aerogels.[71] Moreover, in comparison with the spectrum of PNFs (crosslinked with CA), a weak shoulder at 1730 cm^{-1} was observed, which was attributed to the formation of an intermolecular carbonyl band as a result of the cross-linking reaction between PNFs and CA[59] (Fig. S3, ESI†).

XRD analysis. The XRD profiles of composite aerogel beads and their counterparts (PNFs, Cs, and CNFs) are exhibited in Fig. 5B. The patterns of CNFs (Fig. S4, CNFs, ESI†) revealed three characteristic peaks near the 2θ value of
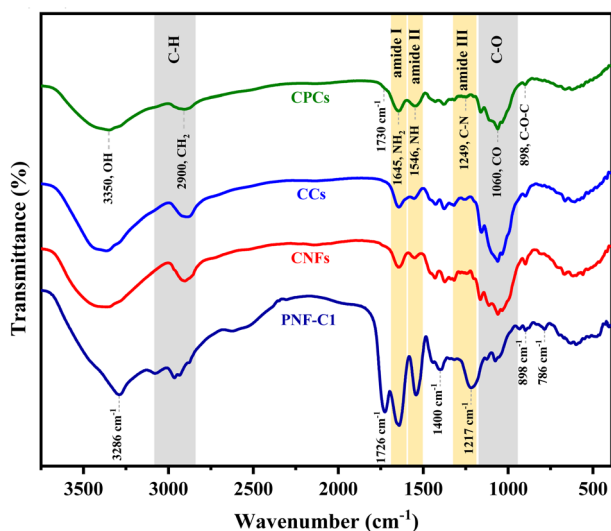

Fig. 5 FTIR spectra of CCs and CPCs composite aerogel beads and their counterparts (CNFs, Cs, and PNFs).

$\sim$13° and 16°, corresponding to cellulose Iβ phase.[72] Conversely, no diffraction peaks were detected for the XRD pattern of PNFs, implying the amorphous nature of Blg (Fig. S4, PNFs, ESI†).[54] The XRD patterns of Cs showed two peaks at 2θ = 10.45°, and 19.83° corresponding to its crystalline and amorphous phases, respectively (Fig. S4, Cs, ESI†).[68,73] Representing two peaks with equal intensity in the 19.8–22.6° region, the hybrid CCs aerogel beads (Fig. S4, CCs, ESI†) exhibited the same characteristic peak as for Cs and CNFs. However, the peak intensity of the CCs aerogel composite decreased significantly compared to pure CNFs, while the peak related to the Cs shifted slightly to 2θ = 20.7°. The diffraction pattern of CPCs was similar to that of a CCs hybrid aerogel, except for the characteristic peak of Cs, which disappeared or weakened after incorporating PNF (Fig. S4, CPCs, ESI†). These findings suggested that PNFs and Cs are well distributed into the CNFs structure, and new intermolecular and intramolecular hydrogen bonds between functional groups of CNFs, Cs, and PNFs were formed.

Adsorption studies. Initially, the adsorption properties of aerogel beads (CPCs) (1 g L^{-1}) for removing various dyes (100 mg L^{-1}) were evaluated. As depicted in Fig. S5 (ESI†), the highest adsorption capacity ($\geq$162 mg g^{-1}) and the maximum dye removal ($\geq$90%) were obtained for the five anionic dyes (AR, RB, CR, DV, and RO). In contrast, the CPCs aerogel exhibited the lowest tendency for adsorption of cationic dyes (CV, MG, BB, CG), with very low values for adsorption capacity ($\leq$31 mg g^{-1}) and removal efficiency ($\leq$15%). These results can be explained by the electrostatic interactions (attraction or repulsion) between the ionic groups of CPCs and dye molecules. Most anionic dyes (*e.g.*, acid, direct, and reactive dyes) contain anionic functional groups, such as hydroxyl, carboxyl, and sulfonic groups, that can be adsorbed to the positively charged groups of CPCs through attractive electrostatic interactions. By contrast, the electrostatic repulsive interactions between the positive groups of cationic dye and the positive surface domain of CPCs were expected to hinder cationic dye adsorption. To further confirm these results, the surface-active charge of CPCs was evaluated at specified pH (7.4) by zeta potential measurements. According to previous reports, CNF suspensions exhibited a negative zeta potential,[74] while the zeta potentials of Cs, and PNF were reported as +4.7 mV,[75] and +48.7 $\pm$ 2.2 mV,[76] respectively. Herein, the Zeta potential of CPCs composite aerogel bead at pH 7.4 was positive (around 47.3 $\pm$ 1.34), pointing out a positively charged surface, attributing to the presence of protonated amine groups (–NH$_3^+$) on the surface of whey PNFs (*e.g.*, protonated histidine, lysine, arginine) and Cs molecules. In light of the above results, incorporating PNFs and Cs in CPCs favours the complete adsorption of anionic dyes from water.[74,75] Remarkably, CPCs aerogel bead demonstrated rapid adsorption in less than 360 min with excellent removal capacity (186 mg g^{-1}), and the highest efficiency (nearly 100%) towards CR of all tested anionic dyes. Thus, to evaluate the capability and performance of aerogel beads in removing dye, the adsorption process of CR as an anionic dye model was investigated in more detail.

The effect of pH. pH directly affects both the adsorbent and the aqueous chemistry and surface charge of the adsorbate. Therefore, we explored the effect of pH on the adsorption capability of CPCs aerogel (1 g L^{-1}) for CR removal (initial concentration of 100 mg L^{-1}) between pH 4 and 10. As the pH of CR solution increased from 4 to 7, the adsorption capacity and removal efficiency increased sharply from 51 mg g^{-1} and 62.54% to 159.77 mg g^{-1} and 95.35%, respectively (Fig. 6A). Notably, the highest adsorption capacity ($\sim$180 mg g^{-1}) with absolute removal efficiency (99.24%) was achieved at pH 7.4, demonstrating the complete discoloration of CR solution.[76] CR (Table S1, ESI†) contains functional groups of –NH$_2$ and –SO$_3$H, and it has a dissociation constant (pK_a) of 3.7;5.5.[77] When the pH value is lower than 4, CR is protonated predominantly, while, at higher pH, it is negatively charged. Additionally, over the pH range of 4 to 7.4, the CPCs aerogel beads positively charged due to the protonated groups (–NH$_3^+$ and –NH$_2^+$), providing favourable sites for the adsorption of anionic sulfated groups (–SO$_3^-$) of CR *via* electrostatic interactions.[78–80] Zeta potential measurements also confirmed the ionic interactions. By contrast, at higher pH values (10 $\geq$ pH $\geq$ 7.4), the number of positively charged sites on the aerogel for CR adsorption declined; thus, the adsorption capacity for CR was reduced. Noticeably, when the pH of the dye solution was adjusted at pH $\geq$8, the amino and carbocyclic acid groups of CPCs were deprotonated. Thus, the interionic repulsion between the negative charge of the adsorbent and anionic sulfonate groups of CR hindered the electrostatic attraction, which caused a gradual drop in the adsorption capacity of CR up to nearly 163.28 mg g^{-1}.[69,75,81] Nevertheless, these results suggested that the CPCs composite aerogel has the potential to be applied in acidic or alkaline medium.

The effect of dosage. The influence of sorbent dosage on the adsorption process was investigated by varying the dosage of aerogels from 1 to 3 g L^{-1} for a fixed CR dye concentration of 1000 mg L^{-1}, at room temperature (28 °C), pH of 7.4, and the shaking speed of 100 rpm. According to Fig. 6B, for both investigated aerogels (CCs or CPCs), the removal efficiency of CR (%) increased from 62% to 100% as the solid content of aerogels increased from 1 to 3 g L^{-1}. Interestingly, the highest adsorption capacity (994 mg g^{-1}) was obtained for 5 mg CPCs aerogel, which was significantly ($\sim$2 times) higher than that of the hybrid composite aerogel of CCs. This result could be ascribed to the presence of PNFs in the composite structure of CPCs, which enhanced the chemical properties of aerogel by introducing a variety of functional groups, particularly additional amino groups. Furthermore, the pores and the active free surface represented a higher affinity to adsorb more CR dyes. As the nanofibers contents of CPCs aerogel increased from 2 to 3 g L^{-1}, even though the surface functional groups of aerogels increased, the adsorption capacity decreased to 461 and 323 mg g^{-1}, respectively. Compared with CCs, the dense structure of CPCs beads consisted of tightly assembled nanofibers, which possibly blocked the partial pores, reduced the porosity, and hindered the flow of CR molecules inside the aerogel core at higher dosages. Thus, the adsorption capacity
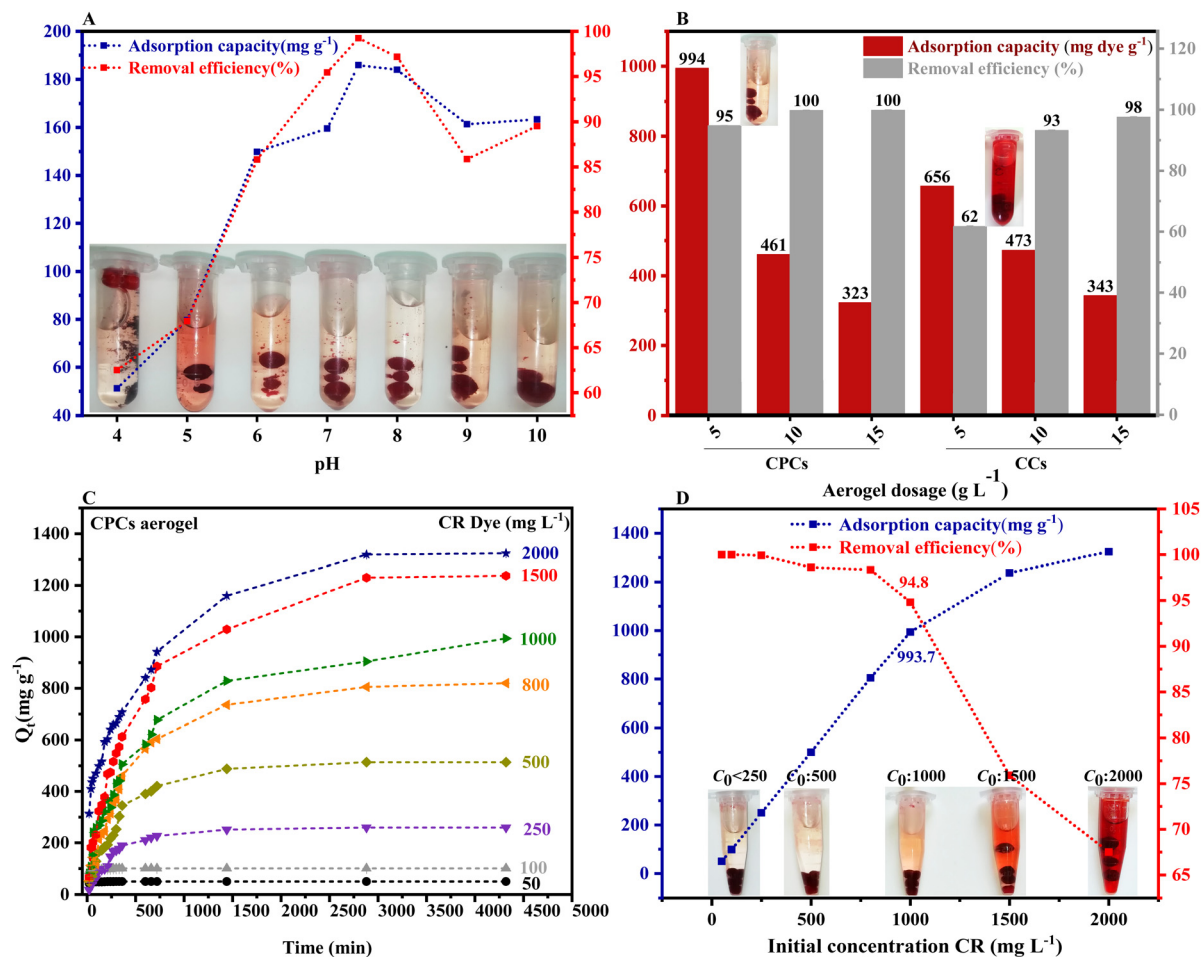
Fig. 6 Evaluating the effect of operational factors on adsorption of CR: (A) Effect of pH (4–10). The inset in (A) illustrating the residual CR dyes after 24 h adsorption process at various Ph. (B) Effect of adsorbent dosage (CPCs and CCs aerogel, 1–3 g L^{-1}). The inset images show the adequate performance of CPCs aerogel bead in CR removal comparing to CCs aerogel beads. (C) Effect of initial CR concentration over time. (D) The equilibrium adsorption capacity and removal efficiency of CR with various concentration (50–2000 mg L^{-1}) onto the CPCs aerogel (1 g L^{-1}) at pH 7.4. The inset pictures exhibit the residual solutions at various dye concentrations in the equilibrium state.

for 2 and 3 g L^{-1} hybrid aerogel of CCs was slightly higher (473 and 343 mg g^{-1}, respectively) than that of the CPCs aerogel (461 and 323 mg g^{-1}, respectively).

The effect of initial CR concentration. Next, we investigated the effect of initial CR concentrations (50–2000 mg L^{-1}) on the adsorption capacity and removal efficiency of the dye on CPCs aerogel. Time-dependent adsorption profiles of CPCs in Fig. 6C and D revealed a rapid adsorption for all CR dye concentrations for the first 6 h, indicating the accessibility of active sites and the large surface area of CPCs aerogel.[69,82] Then, adsorption attained an equilibrium state after 24–30 h. Notably, the adsorption equilibrium time for CR dye with a lower concentration ($\geq$500 mg L^{-1}) was shorter than 3 h. As shown in Fig. 6C, realized that the adsorption capacity increased from 50 to 1323.83 mg g^{-1} as the initial concentration raised from 50 to 2000 mg L^{-1}. In fact, at lower concentrations, higher accessible sites led to the removal of more than 94.8% of the dye. In contrast, the saturation of these active sites at higher dye concentrations resulted in a lower tendency of CPCs aerogel to adsorb more CR molecules (67% of the CR) Fig. 6D.

Effect of contact time. The obtained optimized values (pH 7.4, dye concentration 1000 mg L^{-1}, and adsorbent dosage of 1 g L^{-1}) were used to investigate the equilibrium adsorption time of CR dye by various aerogels (CPCs, CCs, and CNFs). The presented results in Fig. 7A and B showed that the adsorption performance of CR was highly dependent on the composition of aerogels. As shown in Fig. 7A and B, the dye uptake of CR increased in the order of CPCs (994 mg g^{-1}) > CCs (656 mg g^{-1}) > CNFs (226 mg g^{-1}) within the equilibrium time. Surprisingly, the adsorption capacity of CPCs aerogel enhanced significantly, indicating that the functional surface groups of CPCs were highly active and accessible for the adsorption of CR. As illustrated in Fig. 7A (CPCs), the uptake of CR with a concentration of 1000 mg L^{-1} climbed sharply within the initial 600 min. Then, it rose gradually with increasing time until the equilibrium was achieved at almost 60 h. In contrast, the CNFs and CCs aerogels were saturated after approximately 600 and 1440 min, respectively, far shorter than the CPCs. According to the maximum removal efficiency of various aerogels in Fig. 7B, it can be concluded that the lower
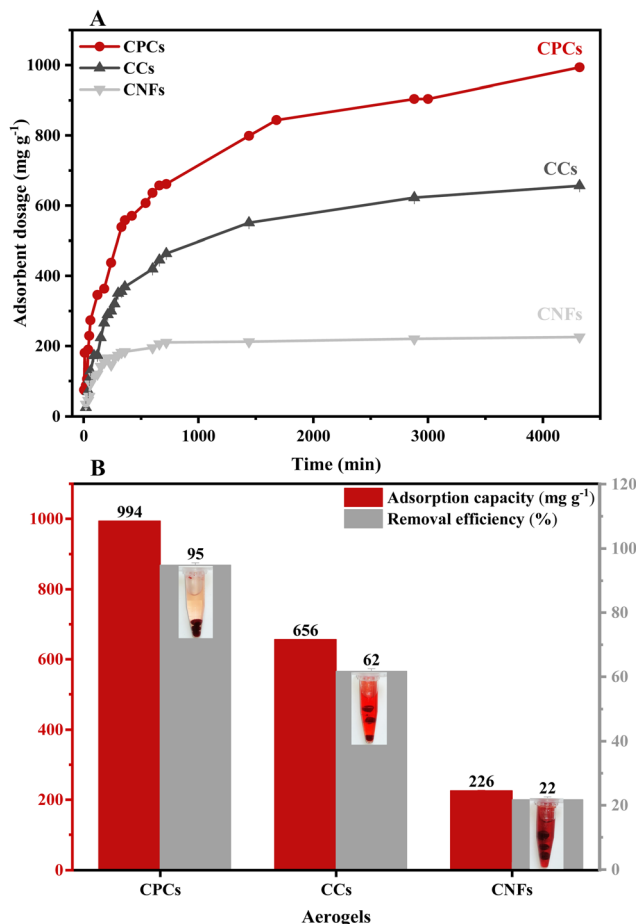
Fig. 7 (A) The effect of contact time on the removal of CR by various aerogel beads, including CNFs, CCs, and CPCs. (B) The equilibrium adsorption and removal efficiency of CNFs, CCs, and CPCs aerogel beads (CR concentration:1000 mg L^{-1}, adsorbent dosage:1 g L^{-1}, pH:7.4). In Fig. 7B, the inset images show the successful removal of CR dye by CPCs aerogel.

values of the CNFs (22%) and CCs (62%) aerogels could be attributed to lower affinity and occupation of active surface sites that led to saturation of aerogels and hindered the adsorption of more CR dye compared to CPCs aerogel with the highest removal efficiency of almost 95%. These results were also confirmed by the remaining CR solutions at equilibrium time. As exhibited in the inset image of Fig. 7B, the color of the CR solution adsorbed by CPCs was nearly colorless, showing that most of the dye molecules were removed from the solution (Inset of Fig. 7B).

Adsorption isotherms. Herein, to understand the adsorption mechanism and to calculate the theoretical maximum adsorption capacity of the adsorbents, the equilibrium adsorption data were analyzed using various isotherm models (*i.e.* Langmuir, Freundlich, Redlich–Peterson, Toth, Temkin, and Sip).[83–87] The non-linear form of all adsorption isotherms and their parameters are presented in Table 1.

The Langmuir model hypothesizes that the adsorbent is homogenous, and the adsorption of a solute from solution occurs at energetically equivalent sites.[88] As presented in Table 1, the Langmuir equation contains two parameters: q_m (mg g^{-1}), the maximum adsorption capacity, and K_L (L mg^{-1}), the Langmuir constant attributed to the apparent energy of sorption. The q_e (mg g^{-1}) and C_e are the equilibrium adsorption capacities and adsorbate concentration.

The Freundlich isotherm model describes multilayer adsorption onto heterogeneous surfaces.[89] The two parameters of the Freundlich equation are K_F (Freundlich constant) and n_F (surface heterogeneity). The $1/n_F$ factor represents the adsorption intensity, indicating the site energy distribution and heterogeneity of the adsorbate. Notably, the adsorption is favorable when $1/n_F$ values are between 0 and 1 ($0 < 1/n_F < 1$).

The Toth isotherm is a modified variant of the Langmuir equation, aiming to improve the fitting by minimizing the error between the experimental data and estimated value.[90]

Table 1 Adsorption isotherm constants for CR adsorption on CPCs aerogel bead

Isotherm model	Formula	Parameter	Values
Two-parameter models			
Langmuir	$q_e = \dfrac{q_m K_L C_e}{1 + K_L C_e}$	q_m [mg g^{-1}] K_L [L mg^{-1}] R^2	1286.61 ± 52.07 0.078 ± 0.015 0.9829
Freundlich	$q_e = K_F C_e^{\frac{1}{n_F}}$	K_F [L mg^{-1}] $1/n_F$ R^2	347.24 ± 53.9 0.23 0.9558
Three-parameter models			
Toth	$q_e = \dfrac{q_m K_t C_e}{[1 + (K_t C_e)^{n_T}]^{\frac{1}{n_T}}}$	q_m [mg g^{-1}] K_T [L mg^{-1}] n_T R^2	794.73 ± 15.13 0.2 ± 0.084 0.91 ± 0.03 0.9926
Redlich–Peterson	$q_e = \dfrac{K_{RP} C_e}{[1 + a_{RP} C_e^{n_{RP}}]}$	K_{RP} [L g^{-1}] a_{RP} [L mg^{-1}] n_{RP} R^2	173.60 ± 46.97 0.23 ± 0.099 0.91 ± 0.03 0.9926
Sip	$q_e = \dfrac{q_m (K_S C_e)^{n_S}}{(1 + K_S C_e)^{n_S}}$	q_m [mg g^{-1}] K_S [L g^{-1}] n_S R^2	1349.77 ± 34.36 0.02 ± 0.0057 0.86 ± 0.059 0.9964

Paper

The K_T (L mg^{-1}), n_T, and q_m (mg g^{-1}) are the Toth constants and maximum adsorption capacity, respectively.

As a hybrid isotherm model, the Redlich–Peterson contains three parameters (K_{RP} (L g^{-1}), n_{RP}, and a_{RP} (L mg^{-1})), which comprise the feature of both Langmuir and Freundlich isotherms.[91,92] The n_{RP} is an exponent which lies between zero and one. When n_{RP} is close to 1, the Redlich–Peterson approaches the Langmuir condition.

Sip isotherm is the combined form of the Langmuir and Freundlich isotherm models, developed to overcome the limitations of increasing adsorbate concentration primarily experienced in the Freundlich isotherm model.[93] The parameters q_m (mg g^{-1}), K_S (L g^{-1}), and n_S are the Sips maximum adsorption capacity and the Sip isotherm constant and exponent, respectively.

The nonlinear fitting of adsorption isotherm models to the equilibrium experimental data, derived from the adsorption of CR onto CPCs composite aerogel, is shown in Fig. 8. The adsorption profile of all isotherm models demonstrated a similar pattern. The predicted isotherm parameters for non-linear models (*i.e.*, two and three-parameter models) are all fully presented in Table 1. Overall, comparison of the value of the correlation coefficient (R^2) (Table 1) that three-parameter models estimated a higher correlation coefficient (>0.992) than two-parameter models.[92] Furthermore, according to the presented data, the non-linearized Sip, Redlich–Peterson, and Langmuir isotherms provided a much better fit to the equilibrium experimental data than Toth and Freundlich isotherms. Among two-parameter models, the correlation coefficient (R^2) value of the Langmuir model (0.982) was higher than that of the Freundlich isotherm (0.955), revealing that the Langmuir isotherm model yielded a better fit. In addition, the maximum adsorption capacity (q_m) obtained by applying the Langmuir model equation was 1286.61 $\pm$ 52.07 mg g^{-1}, which was far from the value predicted by Freundlich isotherm

(347.24 $\pm$ 53.9). Notably, the constant parameter of $1/n_F$ from the Freundlich equation is less than one (0.23), demonstrating that the CR dye is favorably adsorbed by porous CPCs aerogel bead. According to the R^2 value of three-parameter models (Table 1), the correlation coefficient of Sip isotherm was higher (0.996) than the Redlich–Peterson and Toth models, which had equal values (0.9926), suggesting that the adsorption phenomena of CPCs composite bead aerogel are well described by Sip isotherm assumption.[94–96] As shown in Fig. 8, the Sip isotherm curve acceptably fit the experimental data, and the shape of the curve was highly correlated with the characteristic of the Langmuir isotherm model.

Moreover, the Sip isotherm is identified by the heterogeneity factor, n_S, and when $n_S = 1$, the Sip model reduces to Langmuir isotherm.[75,85,97] Herein, the n_S value was 0.9, approximately, demonstrating that the adsorption process of CR dye onto CPCs aerogel bead was homogeneous and referred explicitly to monolayer adsorption. The maximum adsorption capacity calculated from Sip isotherm was 1349.77 $\pm$ 34.36 mg g^{-1}. This high adsorption capacity is resulted from the impregnation of functional biomaterials (PNFs and Cs) into the CPCs composite aerogel, indicating that CPCs have the best capability to remove anionic dye from an aqueous solution. The extent of adsorption obtained from the two parameters of q_m (794.73 $\pm$ 15.13) and the ratio of K_{RP}/a_{RP} (754.8 $\pm$ 10.8) related to Toth and Redlich–Peterson equations, respectively, were comparable.[92,98] Consequently, adsorption mechanism follows the monolayer adsorption of CR dye on a homogeneous surface of CPCs composite aerogel beads, in which all active sites have a similar affinity for the adsorbate.

Adsorption kinetic. The study of adsorption kinetic provides specific information about the rate and mechanism of adsorption, which is crucial for evaluating the adsorption performance of adsorbent.[99] In this study, the experimental kinetic data was analyzed with four well-known kinetic models: (i) nonlinear pseudo-first-order (eqn (1)),[83] (ii) non-linear pseudo-second-order (eqn (2))[100,101] (iii) non-linear Evolich (eqn (3)), and (iv) intraparticle diffusion (Weber and Moris model) (eqn (4)).[102] The kinetic equations are expressed as follows:

$$q_t = q_e(1 - e^{-k_1 t}) \tag{3}$$

$$q_t = \frac{k_2 q_e^2 t}{1 + k_2 q_e t} \text{ and } h = k_2 q_e^2 \tag{4}$$

$$q_t = \frac{1}{\beta}\ln(\alpha\beta t + 1) \tag{5}$$

$$q_t = k_{id} t^{1/2} + C_i \tag{6}$$

where $q_{e,cal}$, and q_t (mg L^{-1}) are the amount of adsorbed CR onto aerogel at equilibrium and at a given time (t) in minutes, respectively; h represents the initial adsorption rate (mg g^{-1} min^{-1}), k_1 (min^{-1}) and k_2 (g mg^{-1} min^{-1}) are the rate constants for pseudo-first-order (PFO) and pseudo-second-
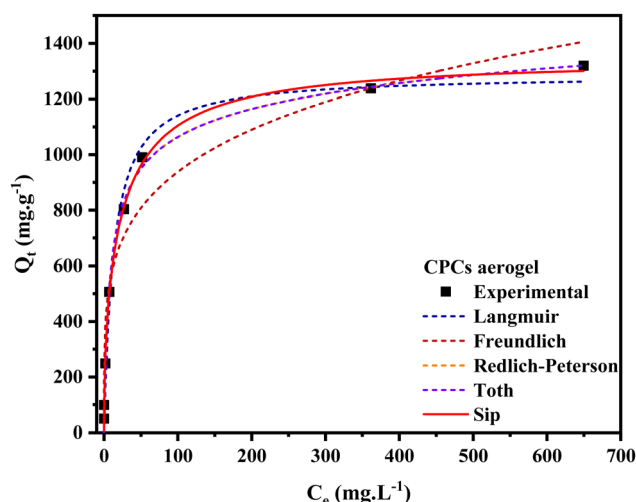

Fig. 8 Nonlinear fitting of adsorption isotherm models to the equilibrium experimental data obtained from the adsorption of the CR onto the CPCs aerogel bead.
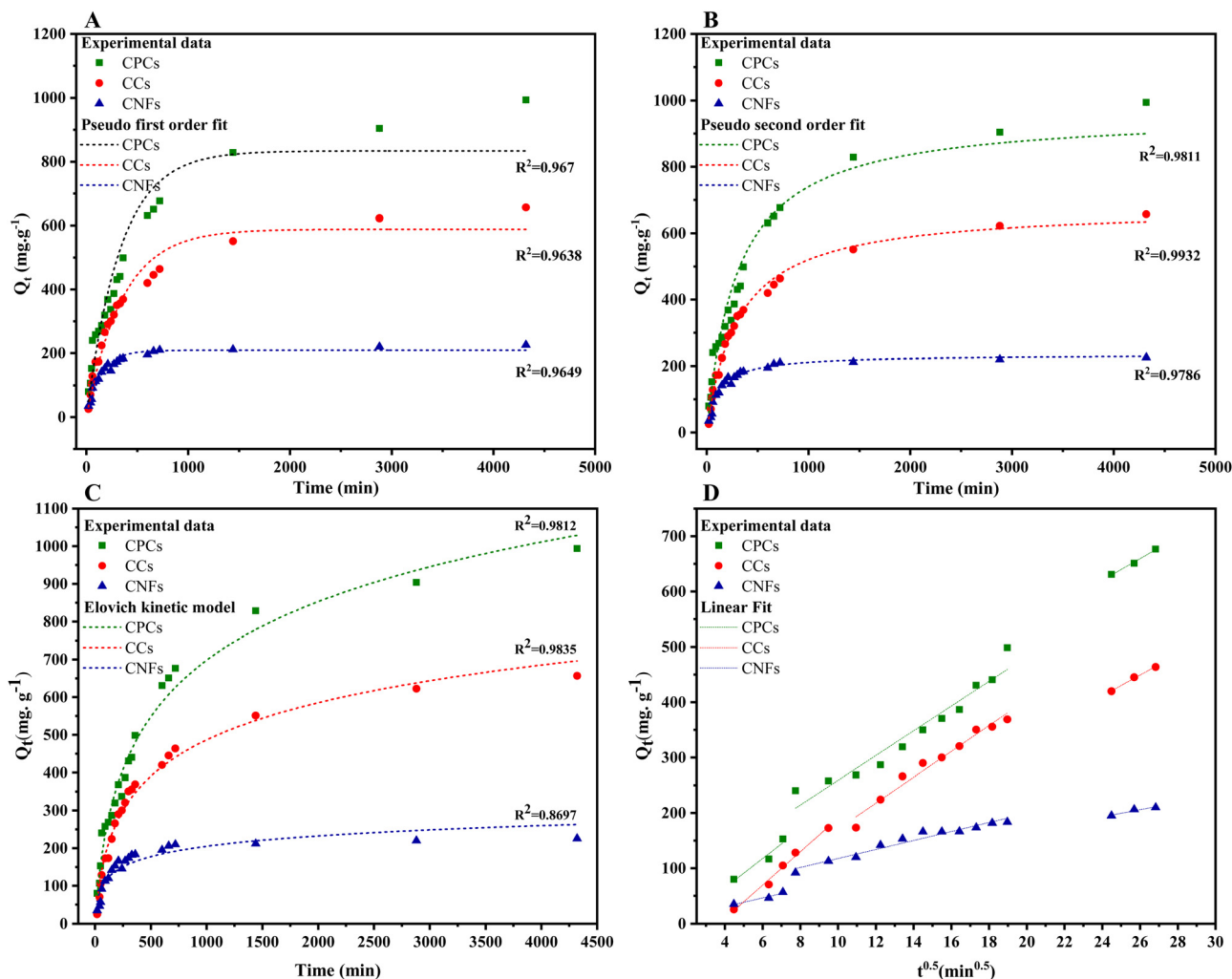
Fig. 9 Kinetic modelling of the adsorption of CR dye (initial concentration of 1000 mg L^{-1}) onto the aerogels with various compositions, *i.e.*, single-component (CNFs), hybrid (CCs), and three-component (CPCs) aerogel composite beads: (A) Pseudo-first-order, (B) Pseudo-second-order, (C) Elovich, (D) intraparticle diffusion models.

order model (PSO), respectively. In fact, in the PFO model, the penetration of adsorbent into the boundary layer is the controlling step. In contrast, chemical adsorption is the governing mechanism in the PSO model and controls the adsorption process. In the Elovich model (eqn (3)), α (mg g^{-1} min^{-1}) is the initial adsorption rate constant, and β (g mg^{-1}) is associated with the extent of surface coverage and activation energy for chemical adsorption. The k_{id} (mg g^{-1} min$^{-0.5}$) is attributed to the rate constant for interparticle diffusion, and C_i (mg g^{-1}) is the intercept related to the thickness of the boundary layer.

Fig. 9 presented the non-linear fitting of PFO, PSO, and the Elovich kinetic models for CR adsorption at the initial concentration of 1000 mg L^{-1} onto aerogels with various compositions, *i.e.*, single-component (CNFs), hybrid (CCs), and three-component (CPCs) aerogel composite beads. Rate constants and other parameters of these kinetic models are summarized in Table 2. The coefficient of determination (R^2) was used to assess the validity of adsorption kinetic models. Among non-linear kinetic models exhibited in Fig. 9A–C, the PSO kinetic

model (Fig. 9B) was fitted well to the experimental data. Moreover, the R^2 value from the non-linear form of the PSO model ($R^2 \geq 0.978$) (Table 2) was higher than those of the PFO ($R^2 \geq 0.965$) and the Elovich models ($R^2 \geq 0.869$), suggesting that CR adsorption onto the aerogel beads (CNFs, CCs, and CPCs) was well expounded by PSO model which means that chemisorption might be the dominating mechanism of adsorption[98,103,104] Furthermore, the theoretical adsorption capacity ($q_{e,cal}$) of all types of aerogels calculated from PSO equation correlated strongly with the experimental adsorption capacity ($q_{e,exp}$, 994 mg g^{-1}) (Table 1). In the case of CPCs aerogel composite bead, for instance, $q_{e,exp}$ was 994 mg g^{-1}; however, the $q_{e,cal}$ value obtained from PFO and PSO equation were 833.74 mg g^{-1} and 962.41 mg g^{-1}, respectively, revealing an insignificant difference between $q_{e,exp}$ and $q_{e,cal}$ in PSO kinetic model. Similarly, the $q_{e,cal}$ values for CCs (679.36 mg g^{-1}) and CNFs (234.41 mg g^{-1}) aerogel beads from PSO were close to their values of $q_{e,exp}$, which were 656 mg g^{-1} and 226 mg g^{-1}, respectively. Notably, the plot of Q_t *vs.* time for all aerogel

Table 2 Kinetic parameters for the adsorption of CR dye using CNFs, CCs, and CPCs composite aerogel beads

| Kinetic model | | Pseudo-first order | | | Pseudo-second order | | | | Elovich | | |
| | | $q_t = q_e \times (1 - e^{K_1 t})$ | | | $q_t = \dfrac{k_2 q_e^2 t}{1 + k_2 q_e t}$ and $h = k_2 q_e^2$ | | | | $q_t = \dfrac{1}{\beta}\ln(\alpha\beta t + 1)$ | | |
		$q_{e,cal}$ [mg g^{-1}]	K_1 [10^{-1} min^{-1}]	R^2	$q_{e,cal}$ [mg g^{-1}]	K_2 [10^{-6}g mg^{-1} min^{-1}]	h mg [g min^{-1}]	R^2	α [mg g^{-1} min^{-1}]	β [g mg^{-1}]	R^2
Adsorbate	CNFs	209	0.07	0.965	234.41	0.4	0.021	0.978	6.89	0.025	0.869
	CCs	588.5	0.03	0.964	679.36	4.81	2.21	0.993	3.944	0.006	0.983
	CPCs	833.74	0.03	0.967	962.41	3.46	3.2	0.981	4.44	0.004	0.971

beads (Fig. 9A–C) exhibited the rapid adsorption of CR on the outer surface of aerogel beads for the first 60 min. Concerning the PSO initial adsorption rate constant, h, the values reported in Table 2 increased as biomaterials such as Cs and PNFs with various functional groups were impregnated in the porous matrix of CNFs aerogel beads (CPCs).[105] In the case of CNFs aerogel beads, for instance, the adsorption rate was around 0.021 (mg g^{-1} min^{-1}); however, the mass transfer rate increased incredibly by almost 313.42% by the addition of Cs and PNFs to the aerogel structure (CPCs). The presence of accessible active sites on the surface of aerogels and the highly porous structure of CPCs aerogel beads provided an excellent affinity for adsorbing higher amounts of CR molecules. Consequently, the adsorption capacity of composite aerogel is enhanced to a greater extent. Thus, these results uncovered the outstanding performance of functionalized CNFs composite aerogel beads complexed with Cs and PNFs.

Overall, adsorption kinetics are governed by multiple subsequent steps, i.e., film diffusion, surface diffusion, and intraparticle diffusion, of which intraparticle diffusion is considered the most rate-limiting step.[87,106] The intraparticle diffusion model (eqn (4)) was used to study the diffusion mechanism, and the calculated results are presented in Fig. 9 and Table 2. The diffusion mechanism includes an initial portion attributed to boundary layer diffusion in which the dye molecules migrate from the bulk solution to the adsorbent and pass a boundary layer, rapid adsorption on the exterior surface of the adsorbent called surface adsorption, followed by a steady adsorption stage where dye molecules enter the pores of the sorbent and are known as the intra-particle diffusion. Lastly, a plateau to equilibrium was attained at the final stage, where the interparticle diffusion tended to reduce as the adsorbate concentration in the solution and accessible adsorption sites decreased.[85,86,107] As shown in Fig. 9, the intra-particle diffusion curve of Q_t versus $t^{0.5}$ exhibited three linear regions for all aerogel beads (i.e., CNFs, CCs, and CPCs) that did not pass

through the origin, expounding three steps governed the adsorption of CR onto the aerogels.

Furthermore, the negative intercept value (C) of the initial line implied minimum boundary-layer resistance. Overall, the k_i value of all aerogels in each step followed the order of $k_{1d} > k_{2d} > k_{3d}$, in which the initial sharp slope (k_{1d}) corresponded to the accelerated migration of CR molecules from the aqueous solution to the exterior surface of aerogels (film or surface diffusion), the second moderate slope (k_{2d}) demonstrated the steady adsorption of CR into the interior surface of porous aerogel beads which was also the rate-controlling step, and k_{3d} represented the final step where the slow diffusion of CR molecules from larger pores into the macro and micro-pores caused a reduction in adsorption rate. According to Table 3, the highest and lowest values of k_{1d} were observed for the CCs (30.3 mg g^{-1}min$^{-0.5}$) and CNFs (8.14 mg g^{-1}min$^{-0.5}$) aerogel beads, respectively. Surprisingly, the value of k_{1d} for CCs hybrid aerogel beads was higher than that (26.5 mg g^{-1}min$^{-0.5}$) of the CPCs composite aerogel beads, indicating that the mass transfer of CR molecule from the solution to the outer surface of hybrid aerogel bead was faster than surface adsorption process of CPCs composite aerogel. In addition, the k_{id} values of CCs aerogel in the second and third stages were about 23 mg g^{-1}min$^{-0.5}$ and 19 mg g^{-1}min$^{-0.5}$, respectively, which were approximately close to the k_{2d} and k_{3d} values obtained for CPCs composite aerogels. Comparing the value of R^2 in the second and third steps, we propose that the mixture of pore diffusion and intra-particle diffusion is the rate-limiting step of the CR adsorption onto the composite aerogel beads[108].

Upon comparing the outcomes of this study to the results of previous research on the adsorption capacities of different adsorbents for CR dye in aqueous solutions, it can be concluded that our results are highly favorable (Table S2, ESI†). All of the data collected were successfully fitted to the pseudo-second-order kinetic model.

Table 3 Intraparticle diffusion model for CR adsorption on CNFs, CCs, and CPCs aerogel beads

| Aerogel | C | First stage | | Second stage | | Third stage | |
		k_{1d} (mg g^{-1}min$^{-0.5}$)	R^2	k_{2d} (mg g^{-1}min$^{-0.5}$)	R^2	k_{3d} (mg g^{-1}min$^{-0.5}$)	R^2
CNFs		8.14 ± 1.88	0.946	7.89 ± 0.59	0.954	6.4 ± 1.7	0.937
CCs		30.27 ± 1.79	0.989	23.38 ± 1.6	0.97	18.814 ± 1.47	0.9939
CPCs		26.49 ± 6.49	0.943	22.34 ± 1.84	0.942	19.59 ± 1.67	0.9927

Study on adsorption mechanism. To better elucidate the intra-particle diffusion process, a morphology study of CPCs aerogel beads was conducted. The FE-SEM micrograph of CPCs aerogel after CR adsorption is shown in Fig. 10A–I. The composite aerogel retained good stability after dye adsorption (Fig. 10A), and the spherical shape of the composite beads remained almost unchanged. Furthermore, the surface morphology of the aerogel bead did not alter much during the dye desorption process (Fig. 10B and C). At low magnification (Fig. 10C and D), the surface morphology of CPCs beads demonstrated porous microstructure containing cellular interconnected pores (Fig. 10D), while FE-SEM images under higher magnification presented assembled fibrils (Fig. 10E). The cross-section of the CPCs beads shown in Fig. 10F–I, demonstrating an integrated robust structure with a porous configuration (Fig. 10G). Notably, the open porous network structure of CPCs beads was well preserved after dye adsorption (Fig. 10H). The morphological results at higher magnification revealed the thin wall of CPCs composite aerogel consisting of a network of entangled individual nanofibrils (Fig. 10I). The FE-SEM -EDX mapping images of CPCs aerogel beads before and after CR adsorption (Fig. S6A and D, ESI†) and their EDX analysis (from the surface (CPCs-Surface) and cross-section (CPCs-Cross)) are presented in Fig. S6G and H (ESI†). The results showed that carbon with content of 55% to 58 wt% was the main element in CPCs aerogel. The elemental mapping of CPCs-Control revealed that Cs and PNFs were uniformly dispersed and combined with CNFs in the aerogel. Furthermore, the atomic percentages of CPCs-Control (Fig. S6B and C, and C-Mapping, ESI†) and CPCs-Cross (Fig. S6E and F, and F-Mapping, ESI†) demonstrated that after dye adsorption, the C, N, and S contents increased by 5.45%, 33.3%, and 300 wt%, respectively. In contrast, the

oxygen content decreased by 17.07 wt% (Fig. S6G and H, ESI†). These findings demonstrate a significant rise in the sulfur content of the aerogel are good evidence that CPCs effectively adsorbed the CR dye.

The FTIR spectra of CPCs before and after adsorption of 1000 mg L^{-1} CR (Fig. 11A, red line), reveal new peaks at 1040, 1175, 1228, and 1373 cm^{-1}, ascribed to S=O stretching of the –SO$_3$ group, while other peaks at 835 and 1459 cm^{-1} are attributed to aromatic backbone vibration of CR.[69,70,109,110] A weak shoulder was observed at 1586 cm^{-1}, attributed to the –N = N- stretching vibration, and the adsorption band of amide I was shifted to a lower wavelength (1618 cm^{-1}).[111] These findings indicated that CR was strongly adsorbed by CPCs composite aerogel.

To verify the above-obtained results, the elemental composition of CPCs aerogel beads was characterized by XPS. As shown in Fig. 11B, the XPS survey spectra of CPCs aerogels before (CPCs-W, Inset image of white aerogel bead) and after adsorption of CR (CPCs-R, Inset image of red aerogel bead) showed similar characteristic peaks of C 1s (285 eV), O 1s (532 eV), and N 1s (399 eV), while the additional peaks at 230 eV (S 2s)[112–115] and 167 eV (S 2p)[116] were only detected for CPCs-R, implying that CR dye molecule was successfully adsorbed on the surface of CPCs aerogel. To obtain detailed information on the elemental composition of the aerogel composite and to compare the changes of the peaks before and after the adsorption of dye, the core peaks of the contained elements (C 1s, O 1s, N 1s, and S p) were separately deconvoluted and shown in Fig. 11B.

The high-resolution C 1s XPS spectrum of CPCs aerogel from Fig. 11B was deconvoluted (Fig. 12A) into five main peak components at 284 eV, 285 eV, 286 eV, 287 eV, and 288 eV, corresponding to the C–C/C–H/C=C, C–N/C–S, C–O, C=O, and
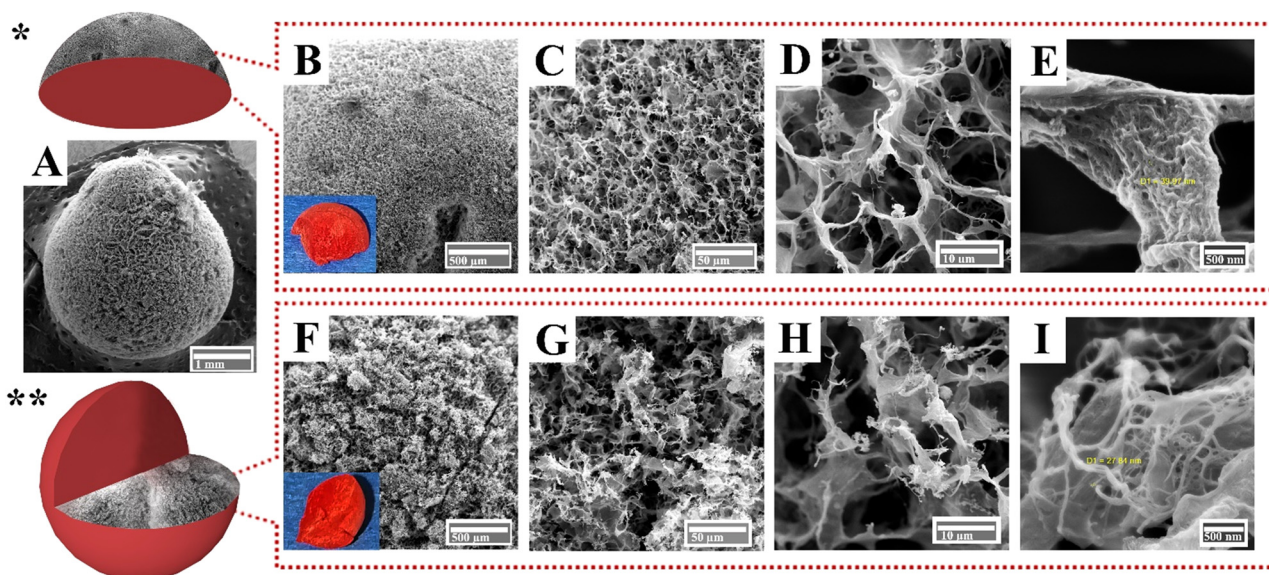

Fig. 10 FE-SEM micrograph of CPCs aerogel after CR adsorption: (A) spherical aerogel (investigating morphologies of aerogel from the *surface and **cross-section directions). (B) Highly porous surface of CPCs aerogel. (C)−(E) High-resolution FESEM images of CPCs porous microstructure containing cellular interconnected pores. (F) The cross-section of CPCs- aerogel bead with integrated robust structure, and (G)−(I) high-resolution FESEM images of CPCs consisting of a network of entangled individual nanofibrils.
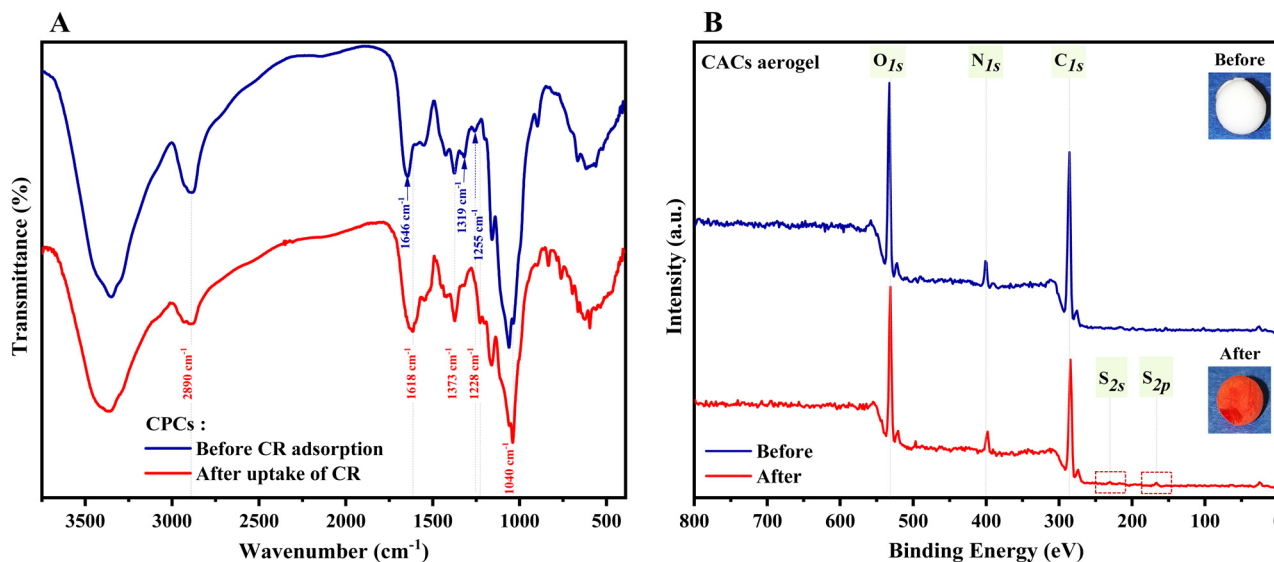
Fig. 11 (A) FTIR and, (B) XPS survey spectra of CPCs aerogel before (blue line) and after (red line) CR adsorption (initial concentration of 1000 mg L^{-1}) at pH = 7.4.

N–C=O, respectively.[82,117] The other weak peaks observed in the spectrum of CPCs-W aerogel at 287.5 eV (C=N) and 290 eV (COOH) disappeared after the adsorption of CR, and instead, new small peaks at 285.6 eV (C=C–N) and 286.47 eV (C–NH$_3^+$, C–N) arose in the spectrum of CPCs-R. The strong peak at 283 eV in the CPCs-R spectra (Fig. 12A) can be related to the C–C/C–H/C=C linkages of adsorbed CR dye. Furthermore, owing to the chemical structure of CR, the dye-adsorbed CPCs composite aerogel had a higher content of the C–N/C–NH$_3^+$ linkages, which might result in overlapping with the C–O functional groups of CPCs-W aerogel and thus weakening of the peak intensity at 286 eV.[118] In Fig. 12A (CPCs-W), the binding energy at ∼289 eV was assigned to the side-chains protonated carboxylic acid groups in glutamic acid and aspartic acid, referring to the incorporation of PNFs into the CNFs/Cs composite aerogel.[119] However, this peak disappeared in the spectrum of CPCs-R, suggesting the formation of hydrogen-bonding interaction between the carboxylic groups of CPCs aerogel and the amine group of CR dye.

A deconvoluted O 1s spectrum of CPCs-W aerogel (Fig. 12B) revealed four peaks at 530.6, 531.9, 533.2, and 535.1 eV, attributed to the COO^{-1}, O=C–O/O=C–N, O=C–O, and O–H (H$_2$O), respectively.[117] Notably, after the adsorption of dye by CPCs aerogel, the spectrum of CPCs-R changed distinctly. In detail, the intensity of characteristic peaks at 530.6 and 535.1 eV decreased, and their peak position shifted to the lower binding energies by 0.3 eV and 0.6 eV. Besides, the carboxylic peak of CPCs-W at 533.2 eV disappeared or might overlap with the critical energy peak of the carbonyl group at 532 eV. These results might be related to the significant contribution of aliphatic carbon, aromatic, and amine groups of CR dye molecules in forming new chemical bonds with active components of CPCs composite aerogel.

The N 1s narrow region spectra of CPCs aerogels (Fig. 12C) were fitted into three sub-peaks at 398.5, 399.7, and 401.1 eV,

which were attributed to N=C–NH, C–N/N=C–NH/O=C–NH, and C–NH$^+$/=N$^+$–, respectively.[47,96] The high-resolution spectrum of N 1s verified the amino acid sequences of the nanofibril protein (including His, Glu, Asp, Ala, Tyr, and Cys). His' imidazole group was verified by lower N 1s binding energies at 398.5 eV for C=N and at 399.7 eV for C–NH.[120] In addition, His revealed a third N 1s signal at 401.4 eV, which could be related to the α-amine nitrogen, in line with the data of protonated α-nitrogen for other amino acids sequences such as Gly, Glu and Asp.

A comparison of the changes in N 1s spectrum before and after CR dye adsorption (Fig. 12C) reveals that the intensity of the peak component belonging to C–NH$^+$ (amine) and O=C–NH (amide) decreased, and the oxidation state (–N=) at 397.7 eV increased. These results proved the presence of active functional groups in the structure of CPCs composite aerogel. They verified the formation of a chemical bond between the sulfite (–SO$_3^{-2}$) groups of dye molecule and protonated amine (–NH$_3^+$/=N$^+$–) groups of CPCs composite aerogel[47].

The deconvolution of the high-resolution S 2P spectra of CPCs composite aerogel bead before adsorption of CR (Fig. 12D) gave rise to peaks at 163 eV and 164.23 eV, accounting for the unbound thiols (S–H bonds), and disulfides (–S–S–), respectively.[121,122] Protein nanofibrils have cysteine residues containing thiol groups at the C-terminus, which can either interact to form intra- and inter-molecular disulfide linkages (sulfur-sulfur) or may remain as free thiols.[121] Moreover, owing to the oxidation phenomenon of the surface, thiosulfate (–S$_2$O$_3^{2-}$) species with an S 2p2/3 binding energy of 168.7 eV was also observed in the spectrum of CPCs-W. Interestingly, after the dye adsorption, a new strengthened peak with an S 2p1/2 binding energy at 167 eV arose in the CPCs-R aerogel spectrum (Fig. 12D). This characteristic peak was assigned to the sulfonate moieties (–SO$_3^-$) of the CR dye molecule. These
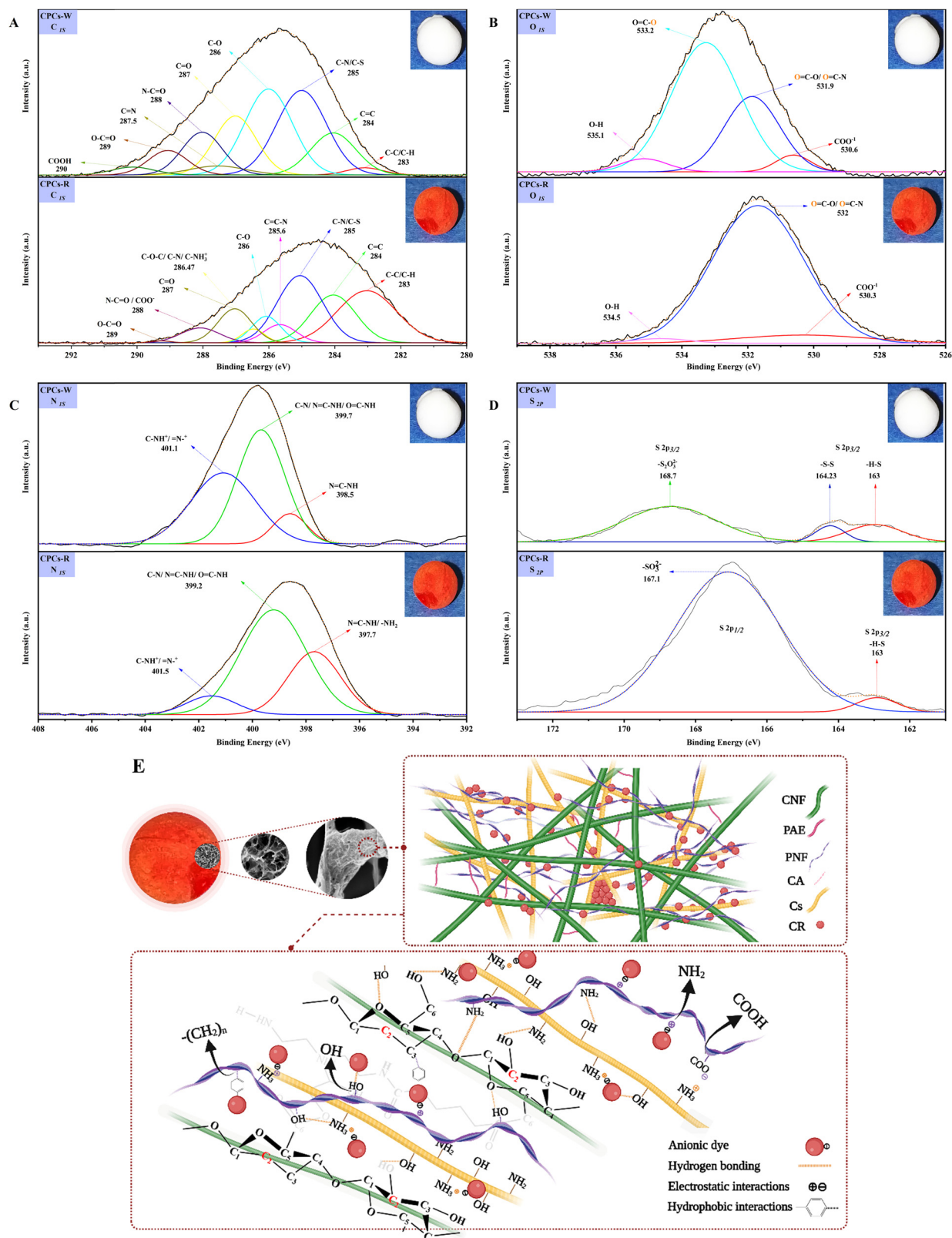
Fig. 12 High-resolution XPS spectra of (A) C_{1s}, (B) O_{1s}, (C) N_{1s}, and (D) S_{1p} of CPCs aerogel before and after CR adsorption at pH = 7.4, (CPCs-W, the inset image indicates the white CPCs aerogel bead as control sample) (CPCs-R, the inset image represents the aerogel bead after adsorption), (E) schematic representation of the binding of CR on to the CPCs aerogel surface.

results suggested that the sulfur element with the S 2p1/2 photoemission signal at 167 eV was the predominant element involved in the solid electrostatic interactions with the protonated amine ($-NH_3^+$) groups of CPCs aerogel[96].

Adsorption mechanism. Based on our data, we propose multiple adsorption mechanisms for the adsorption of CR by the CPCs aerogel (Fig. 12E). The CPCs aerogel is composed of a variety of biopolymers (*i.e.*, crosslinked CNFs, Cs, and crosslinked PNFs) with a large number of binding sites provided by *inter alia* hydroxyl, carboxyl, guanidine, amine, amide and thiol groups. When the dye is below its isoelectric point, it primarily exists in its molecular form. However, above the isoelectric point, it predominantly takes on its dissociated form. In the case of CR (with an isoelectric point of 3), it becomes negatively charged within the pH range of 5.0–10.0.[81] The calculated zeta-potential value for CPCs (47.3 ± 1.3) revealed that the adsorbent surface had a positive charge under neutral conditions. Adding Cs and PNFs to the matrix of CNFs, the chemical composition of the aerogel was enriched with amine groups. The amine groups were positively charged NH^{3+} with the ionized H^+ in the aqueous solution. Besides, CR is an acidic diazo dye containing sulfonic groups ($-SO_3H$), forming negatively charged ($-SO_3^-$) in an aqueous solution,[81] and thus attracted electrostatically to the positively surface amine groups of CPCs aerogel.[123,124] Additionally, specific molecular components of CR, such as N, S, O, benzene ring, and CH_2OH groups in the chitosan molecule, have the potential for hydrogen bond formation (Table S1 and Fig. 12E, ESI†). Moreover, the electronegative hydrogen atoms of the CR can form hydrogen bonds with the electronegative oxygen (from carboxyl and hydroxyl groups) and nitrogen (from amine groups) of the CPCs aerogel. Apart from this, the aromatic backbone of CR dye can interact with the carbohydrate C–H bonds and form CH–π interactions.[125] Consequently, the physical structure of CPCs aerogel bead, investigated through FE-SEM and BET analysis, demonstrated that the increased specific surface area, high porosity, and the microchannel orientation of the aerogel bead enhanced the diffusion of CR molecule into the pore and inner surface. In brief, strong electrostatic interactions, hydrogen bonds, CH–π and π–π bonds, and the mesoporous structure of the aerogel bead make CPC aerogels a high-performance adsorbent for removing pollutants from water.

Conclusions

We have developed a green porous aerogel composed of whey protein nanofibers/cellulose nanofibers/chitosan through the facile procedure of ice-templating. Zeta potential analysis revealed a positively charged surface at pH 7.4, nearly 47.3 ± 1.34, which may be attributed to protonated amine groups ($-NH3^+$) on the surface of Cs molecules and whey PNFs. Morphological studies revealed that the spherical CPCs aerogel had a specified center-diverging microchannel structure. The results of BET were consistent with the FE-SEM observations, implying that the CPCs aerogel has a porous structure

consisting of mesoporous and flexible thin walls, which endowed the CPCs aerogel with enhanced adsorption capacity and rapid mass transportation of liquid. The maximum adsorption capacity calculated from Sip isotherm was 1349.77 ± 34.36 mg g^{-1}, demonstrating that the adsorption process of CR dye onto CPCs aerogel bead was homogeneous and referred explicitly to monolayer adsorption. The interconnected pore channels found in CPCs aerogel provided abundant transport pathways, allowing for efficient separation and elimination of dye molecules. In contrast, the inclusion of functional groups within these channels facilitates their interaction with specific moieties. Our adsorption studies suggest that the mixture of pore diffusion and intra-particle diffusion might be the rate-limiting step of the CR adsorption onto the composite aerogel beads. Consequently, CPCs composite aerogel beads with homogeneous surface and active sites have a high potential to remove pollutants from wastewater.

Abbreviation

βLG	β-Lactoglobulin
CA	Citric acid
CCs	CNFs/Cs aerogel beads
CNFs	Cellulose nanofibers
CR	Congo red
Cs	Chitosan
CPCs	CNFs/Cs/PNFs aerogel beads
PAE	Polyamideamine-epichlorohydrin
PNFs	Protein nanofibrils
PNFs-C	Cross-linked protein fibrils
ThT	thioflavin T
WPI	Whey protein isolate

Author contributions

Mandana Dilamian: conceptualization, methodology, investigation, writing – review & editing. Majid Montazer: validation, writing – review & editing. Hossein Yousefi: Validation, writing – review & editing. Daniel E. Otzen: validation, writing – review & editing, funding acquisition. Dina Morshedi: conceptualization, methodology, supervision, writing – review & editing, funding acquisition.

Data availability

The datasets generated during and/or analysed during the current study are not publicly available due to commercial reasons but the basic description of data types are available at: cellulose nanofibers/protein nanofibrils nanocomposite aerogels: preparation and characterization.

Conflicts of interest

There are no conflicts to declare.

Acknowledgements

References

1 J. Wang and S. Zhuang, Removal of various pollutants from water and wastewater by modified chitosan adsorbents, *Crit. Rev. Environ. Sci. Technol.*, 2017, **47**(23), 2331.

2 M. N. Faiz Norrrahim, N. A. Mohd Kasim, V. F. Knight, M. S. Mohamad Misenan, N. Janudin and N. A. Ahmad Shah, *et al.*, Nanocellulose: a bioadsorbent for chemical contaminant remediation, *RSC Adv.*, 2021, **11**(13), 7347.

3 F. Jiang, D. M. Dinh and Y. L. Hsieh, Adsorption and desorption of cationic malachite green dye on cellulose nanofibril aerogels, *Carbohydr. Polym.*, 2017, **173**, 286.

4 D. Morshedi, Z. Mohammadi, M. M. A. Boojar and F. Aliakbari, Using protein nanofibrils to remove azo dyes from aqueous solution by the coagulation process, *Colloids Surf., B*, 2013, **112**, 245.

5 T. Hou, K. Guo, Z. Wang, X. F. Zhang, Y. Feng and M. He, *et al.*, Glutaraldehyde and polyvinyl alcohol crosslinked cellulose membranes for efficient methyl orange and Congo red removal, *Cellulose*, 2019, **26**, 5065.

6 N. Ali, A. Said, F. Ali, F. Raziq, Z. Ali and M. Bilal, *et al.*, Photocatalytic degradation of congo red dye from aqueous environment using cobalt ferrite nanostructures: development, characterization, and photocatalytic performance, *Water, Air, Soil Pollut.*, 2020, **231**, 1–16.

7 D. N. Ahmed, L. A. Naji, A. A. H. Faisal, N. Al-Ansari and M. Naushad, Waste foundry sand/MgFe-layered double hydroxides composite material for efficient removal of Congo red dye from aqueous solution, *Sci. Rep.*, 2020, **10**(1), 2042.

8 N. P. Shetti, S. J. Malode, R. S. Malladi, S. L. Nargund, S. S. Shukla and T. M. Aminabhavi, Electrochemical detection and degradation of textile dye Congo red at graphene oxide modified electrode, *Microchem. J.*, 2019, **146**, 387.

9 U. J. Kim, S. Kimura and M. Wada, Highly enhanced adsorption of Congo red onto dialdehyde cellulose-crosslinked cellulose-chitosan foam, *Carbohydr. Polym.*, 2019, **214**, 294–302.

10 J. You, C. Liu, X. Feng, B. Lu, L. Xia and X. Zhuang, In situ synthesis of ZnS nanoparticles onto cellulose/chitosan sponge for adsorption–photocatalytic removal of Congo red, *Carbohydr. Polym.*, 2022, **288**, 119332.

11 L. E. Nita, A. Ghilan, A. G. Rusu, I. Neamtu and A. P. Chiriac, New Trends in Bio-Based Aerogels, *Pharmaceutics*, 2020, **12**(5), 449.

12 M. Peydayesh, J. Vogt, X. Chen, J. Zhou, F. Donat and M. Bagnani, *et al.*, Amyloid-based carbon aerogels for water purification, *Chem. Eng. J.*, 2022, **449**, 137703.

13 D. M. Guo, Q. D. An, Z. Y. Xiao, S. R. Zhai and D. J. Yang, Efficient removal of Pb (II), Cr (VI) and organic dyes by polydopamine modified chitosan aerogels, *Carbohydr. Polym.*, 2018, **202**, 306.

14 D. P. Stephen and S. B. Palanisamy, Advances in biopolymer composites and biomaterials for the removal of emerging contaminants, *Phys. Sci. Rev.*, 2023, **8**(8), 1789.

15 K. Ganesan, T. Budtova, L. Ratke, P. Gurikov, V. Baudron and I. Preibisch, *et al.*, Review on the production of polysaccharide aerogel particles, *Materials*, 2018, **11**(11), 1–37.

16 M. A. Shahbazi, M. Ghalkhani and H. Maleki, Directional Freeze-Casting: A Bioinspired Method to Assemble Multifunctional Aligned Porous Structures for Advanced Applications, *Adv. Eng. Mater.*, 2020, **22**(7), 2000033.

17 M. Dilamian and B. Noroozi, Rice straw agri-waste for water pollutant adsorption: Relevant mesoporous super hydrophobic cellulose aerogel, *Carbohydr. Polym.*, 2021, **251**, 117016.

18 M. Zhang, M. Li, Q. Xu, W. Jiang, M. Hou and L. Guo, *et al.*, Nanocellulose-based aerogels with devisable structure and tunable properties via ice-template induced self-assembly, *Ind. Crops Prod.*, 2022, **179**, 114701.

19 F. Zhao, L. Lin, J. Zhang, J. Liu, J. Shi and Y. L. Godec, *et al.*, Ice-Templating: Integrative Ice Frozen Assembly to Tailor Pore Morphology of Energy Storage and Conversion Devices, *Adv. Mater. Technol.*, 2023, **2201968**, 1–25.

20 S. Ahmad, W. A. Siddiqi and S. Ahmad, Sustainable nanocomposite porous absorbent and membrane sieves: Definition, classification, history, properties, synthesis, applications, and future prospects, *J. Environ. Chem. Eng.*, 2023, **11**(2), 109367.

21 S. Liao, T. Zhai and H. Xia, Highly adsorptive graphene aerogel microspheres with center-diverging microchannel structures, *J. Mater. Chem. A*, 2016, **4**(3), 1068.

22 Q. Guo, E. Amendola, M. Lavorgna, Z. Li, H. Feng and Y. Wu, *et al.*, Robust and recyclable graphene/chitosan composite aerogel microspheres for adsorption of oil pollutants from water, *Carbohydr. Polym.*, 2022, **290**, 119416.

23 H. Qin, Y. Zhang, J. Jiang, L. Wang, M. Song and R. Bi, *et al.*, Multifunctional Superelastic Cellulose Nanofibrils Aerogel by Dual Ice-Templating Assembly, *Adv. Funct. Mater.*, 2021, **31**(46), 2106269.

24 N. Rong, C. Chen, K. Ouyang, K. Zhang, X. Wang and Z. Xu, Adsorption characteristics of directional cellulose nanofiber/chitosan/montmorillonite aerogel as adsorbent for wastewater treatment, *Sep. Purif. Technol.*, 2021, **274**, 119120.

25 J. Wang, Q. Yao, C. Sheng, C. Jin and Q. Sun, One-Step Preparation of Graphene Oxide/Cellulose Nanofibril Hybrid Aerogel for Adsorptive Removal of Four Kinds of Antibiotics, *J. Nanomater.*, 2017, **2017**, 5150613.

26 H. Cai, S. Sharma, W. Liu, W. Mu, W. Liu and X. Zhang, *et al.*, Aerogel Microspheres from Natural Cellulose Nanofibrils and Their Application as Cell Culture Scaffold, *Biomacromolecules*, 2014, **15**(7), 2540.

27 H. S. H. Nguyen, K. Phuong and T. Nguyen, Insights into sustainable aerogels from lignocellulosic materials, *J. Mater. Chem. A*, 2022, **10**(44), 23467.

28 Y. Lv, Z. Liang, Y. Li, Y. Chen, K. Liu and G. Yang, *et al.*, Efficient adsorption of diclofenac sodium in water by a novel functionalized cellulose aerogel, *Environ. Res.*, 2021, **194**, 110652.

29 Q. Wang, W. Zuo, Y. Tian, L. Kong, G. Cai and H. Zhang, *et al.*, Chemosphere An ultralight and flexible nanofibril-lated cellulose/chitosan aerogel for efficient chromium removal: Adsorption-reduction process and mechanism, *Chemosphere*, 2023, **329**, 138622.

30 D. M. Guo, Q. D. An, R. Li, Z. Y. Xiao and S. R. Zhai, Ultrahigh selective and efficient removal of anionic dyes by recyclable polyethylenimine-modified cellulose aerogels in batch and fixed-bed systems, *Colloids Surf., A*, 2018, **555**, 150.

31 N. P. Raval, P. U. Shah, D. G. Ladha, P. M. Wadhwani and N. K. Shah, Comparative study of chitin and chitosan beads for the adsorption of hazardous anionic azo dye Congo Red from wastewater, *Desalin. Water Treat.*, 2016, **57**(20), 9247.

32 A. Sowmya and S. Meenakshi, An efficient and regenerable quaternary amine modified chitosan beads for the removal of nitrate and phosphate anions, *J. Environ. Chem. Eng.*, 2013, **1**(4), 906.

33 A. Pei, N. Butchosa, L. A. Berglund and Q. Zhou, Surface quaternized cellulose nanofibrils with high water absor-bency and adsorption capacity for anionic dyes, *Soft Matter*, 2013, **9**(6), 2047.

34 U. J. Kim, D. Kim, J. You, J. W. Choi, S. Kimura and M. Wada, Preparation of cellulose-chitosan foams using an aqueous lithium bromide solution and their adsorption ability for Congo red, *Cellulose*, 2018, **25**(4), 2615.

35 Y. Wang, H. Wang, H. Peng, Z. Wang, J. Wu and Z. Liu, Dye Adsorption from Aqueous Solution by Cellulose/Chitosan Composite: Equilibrium, Kinetics, and Thermodynamics, *Fibers Polym.*, 2018, **19**(2), 340.

36 S. Rahimi Aqdam, D. E. Otzen, N. M. Mahmoodi and D. Morshedi, Adsorption of azo dyes by a novel bio-nanocomposite based on whey protein nanofibrils and nano-clay: Equilibrium isotherm and kinetic modeling, *J. Colloid Interface Sci.*, 2021, **602**, 490–503.

37 Q. Zhang, S. Zhang, Z. Zhao, M. Liu, X. Yin and Y. Zhou, *et al.*, Highly effective lead (II) removal by sustainable alkaline activated β-lactoglobulin nanofibrils from whey protein, *J. Cleaner Prod.*, 2020, **255**, 120297.

38 C. Lendel and N. Solin, Protein nanofibrils and their use as building blocks of sustainable materials, *RSC Adv.*, 2021, **11**(62), 39188.

39 M. Peydayesh, M. K. Suter, S. Bolisetty, S. Boulos, S. Handschin and L. Nyström, *et al.*, Amyloid Fibrils Aerogel for Sustainable Removal of Organic Contaminants from Water, *Adv. Mater.*, 2020, **32**(12), 1–6.

40 J. Fu, F. Yang and Z. Guo, The chitosan hydrogels: From structure to function, *New J. Chem.*, 2018, **42**(21), 17162.

41 M. Tan, H. Lv, Q. Zhao, B. Wang, S. Zheng and K. Li, Chitosan–Quinoa Bran Aerogel: A Low-Cost, Highly-Efficient, and Recyclable Adsorbents for Wastewater Treat-ment, *Environ. Eng. Sci.*, 2023, **40**(6), 233.

42 Y. Mansourpanah, Nanofiltration membranes, *J. Membr. Sci. Res.*, 2017, **3**(1), 1.

43 L. Severini, K. J. De France, D. Sivaraman, N. Kummer and G. Nyström, Biohybrid Nanocellulose–Lysozyme Amyloid Aerogels via Electrostatic Complexation, *ACS Omega*, 2022, **7**(1), 578.

44 X. Ye, K. Junel, M. Gällstedt, M. Langton, X. F. Wei and C. Lendel, *et al.*, Protein/Protein Nanocomposite Based on Whey Protein Nanofibrils in a Whey Protein Matrix, *ACS Sustainable Chem. Eng.*, 2018, **6**(4), 5462.

45 Y. Zhang, J. Hua, M. Zhao, H. Wu, Y. Shao and M. Zhou, *et al.*, 1-(2-pyridylazo) 2-naphthol-modified bacterial cellu-lose/multiwall carbon nanotube/silicon dioxide membrane for selectively adsorbed Er(III), *Fullerenes, Nanotubes Carbon Nanostruct.*, 2023, **31**(3), 288.

46 S. Bolisetty, N. M. Coray, A. Palika, G. A. Prenosil and R. Mezzenga, Amyloid hybrid membranes for removal of clinical and nuclear radioactive wastewater, *Environ. Sci.*, 2020, **6**(12), 3249.

47 Y. Zhang, J. Wen, Y. Zhou, J. Wang and W. Cheng, Novel efficient capture of hexavalent chromium by polyethylenei-mine/amyloid fibrils/polyvinyl alcohol aerogel beads: Functional design, applicability, and mechanisms, *J. Hazard. Mater.*, 2023, **458**, 132017.

48 S. V. Kamath, M. H. Mruthunjayappa, D. Mondal and N. Sanna Kotrappanavar, Nanocomposite-based high-performance adsorptive water filters: recent advances, limitations, nanotoxicity and environmental implications, *Environ. Sci.: Nano*, 2022, **9**(7), 2320.

49 G. Nyström, W. K. Fong and R. Mezzenga, Ice-Templated and Cross-Linked Amyloid Fibril Aerogel Scaffolds for Cell Growth, *Biomacromolecules*, 2017, **18**(9), 2858.

50 M. Peydayesh, T. Greber, I. Haechler, A. Armanious, X. Jia and M. Usuelli, *et al.*, Renewable Water Harvesting by Amyloid Aerogels and Sun, *Adv. Sustainable Syst.*, 2022, **6**(1), 2100309.

51 M. Peydayesh, M. K. Suter, S. Bolisetty, S. Boulos, S. Handschin and L. Nyström, *et al.*, Amyloid Fibrils Aerogel for Sustainable Removal of Organic Contaminants from Water, *Adv. Mater.*, 2020, **32**(12), 1–6.

52 L. Severini, K. J. De France, D. Sivaraman, N. Kummer and G. Nyström, Biohybrid Nanocellulose–Lysozyme Amyloid Aerogels via Electrostatic Complexation, *ACS Omega*, 2022, **7**(1), 578.

53 M. Usuelli, T. Germerdonk, Y. Cao, M. Peydayesh, M. Bagnani and S. Handschin, *et al.*, Polysaccharide-reinforced amyloid fibril hydrogels and aerogels, *Nanoscale*, 2021, **13**(29), 12534.

54 M. Peydayesh, X. Chen, J. Vogt, F. Donat, C. R. Müller and R. Mezzenga, Amyloid fibril-UiO-66-NH$_2$ aerogels for environmental remediation, *Chem. Commun.*, 2022, **58**(33), 5104.

55 G. Nyström, L. Roder, M. P. Fernández-Ronco and R. Mezzenga, Amyloid Templated Organic–Inorganic Hybrid Aerogels, *Adv. Funct. Mater.*, 2018, **28**(27), 1–11.

56 M. Dilamian and D. Morshedi, Cellulose nanofibers/protein nanofibrils nanocomposite aerogels: Preparation and characterization, *J. Wood Forest Sci. Technol.*, 2022, **29**(4), 113.

57 B. Ma, X. You and F. Lu, Inhibitory effects of β-ionone on amyloid fibril formation of β-lactoglobulin, *Int. J. Biol. Macromol.*, 2014, **64**, 162.

58 S. Brunauer, P. H. Emmett and E. Teller, Adsorption of Gases in Multimolecular Layers, *J. Am. Chem. Soc.*, 1938, **60**(2), 309.

59 G. Nyström, W. K. Fong and R. Mezzenga, Ice-Templated and Cross-Linked Amyloid Fibril Aerogel Scaffolds for Cell Growth, *Biomacromolecules*, 2017, **18**(9), 2858.

60 H. Zhang, I. Hussain, M. Brust, M. F. Butler, S. P. Rannard and A. I. Cooper, Aligned two- and three-dimensional structures by directional freezing of polymers and nanoparticles, *Nat. Mater.*, 2005, **4**(10), 787.

61 W. Shi, Y. C. Ching and C. H. Chuah, Preparation of aerogel beads and microspheres based on chitosan and cellulose for drug delivery: A review, *Int. J. Biol. Macromol.*, 2021, **170**, 751.

62 M. He, G. Fei, Z. Zheng, Z. Cheng, Z. Wang and H. Xia, Pt Nanoparticle-Loaded Graphene Aerogel Microspheres with Excellent Methanol Electro-Oxidation Performance, *Langmuir*, 2019, **35**(10), 3694.

63 R. Yu, Y. Shi, D. Yang, Y. Liu, J. Qu and Z. Z. Yu, Graphene Oxide/Chitosan Aerogel Microspheres with Honeycomb-Cobweb and Radially Oriented Microchannel Structures for Broad-Spectrum and Rapid Adsorption of Water Contaminants, *ACS Appl. Mater. Interfaces*, 2017, **9**(26), 21809.

64 K. S. W. Sing, Reporting physisorption data for gas/solid systems with special reference to the determination of surface area and porosity (Recommendations 1984), *Pure Appl. Chem.*, 1985, **57**(4), 603.

65 J. Rouquerol, D. Avnir, C. W. Fairbridge, D. H. Everett, J. M. Haynes and N. Pernicone, *et al.*, Recommendations for the characterization of porous solids (Technical Report), *Pure Appl. Chem.*, 1994, **66**(8), 1739.

66 M. Di Foggia, P. Taddei, A. Torreggiani, M. Dettin and A. Tinti, Self-assembling peptides for biomedical applications: IR and Raman spectroscopies for the study of secondary structure, *Proteomics Res. J.*, 2011, **2**(3), 231.

67 P. Singh and R. Kaur, One pot synthesis of bio-based porous isocyanate-free polyurethane materials, *Mater. Lett.*, 2023, **331**, 133433.

68 Y. Wang, H. Wang, H. Peng, Z. Wang, J. Wu and Z. Liu, Dye Adsorption from Aqueous Solution by Cellulose/Chitosan Composite: Equilibrium, Kinetics, and Thermodynamics, *Fibers Polym.*, 2018, **19**(2), 340.

69 U. J. Kim, D. Kim, J. You, J. W. Choi, S. Kimura and M. Wada, Preparation of cellulose-chitosan foams using an aqueous lithium bromide solution and their adsorption ability for Congo red, *Cellulose*, 2018, **25**(4), 2615.

70 Y. Xinxin, Y. Li, H. Gao, C. Wang, X. Zhang and H. Zhou, One-step fabrication of chitosan-Fe(OH)3 beads for efficient adsorption of anionic dyes, *Int. J. Biol. Macromol.*, 2018, **117**, 30–41.

71 M. Peydayesh, M. K. Suter, S. Bolisetty, S. Boulos, S. Handschin and L. Nyström, *et al.*, Amyloid Fibrils Aerogel for Sustainable Removal of Organic Contaminants from Water, *Adv. Mater.*, 2020, **32**(12), 1–6.

72 M. Dilamian and B. Noroozi, Rice straw agri-waste for water pollutant adsorption: Relevant mesoporous super hydrophobic cellulose aerogel, *Carbohydr. Polym.*, 2021, **251**, 117016.

73 H. Tu, Y. Yu, J. Chen, X. Shi, J. Zhou and H. Deng, *et al.*, Highly cost-effective and high-strength hydrogels as dye adsorbents from natural polymers: chitosan and cellulose, *Polym. Chem.*, 2017, **8**(19), 2913.

74 M. Peydayesh and R. Mezzenga, Protein nanofibrils for next generation sustainable water purification, *Nat. Commun.*, 2021, **12**(1), 3248.

75 Y. Liu, Y. Ke, Q. Shang, X. Yang, D. Wang and G. Liao, Fabrication of multifunctional biomass-based aerogel with 3D hierarchical porous structure from waste reed for the synergetic adsorption of dyes and heavy metal ions, *Chem. Eng. J.*, 2023, **451**, 138934.

76 U. J. Kim, H. J. Kim, J. W. Choi, S. Kimura and M. Wada, Cellulose-chitosan beads crosslinked by dialdehyde cellulose, *Cellulose*, 2017, **24**(12), 5517.

77 C. Wu, J. Scott and J. E. Shea, Binding of Congo red to amyloid protofibrils of the Alzheimer Aβ(9-40) peptide probed by molecular dynamics simulations, *Biophys. J.*, 2012, **103**(3), 550.

78 C. Q. Ruan, M. Stromme and J. Lindh, Preparation of porous 2,3-dialdehyde cellulose beads crosslinked with chitosan and their application in adsorption of Congo red dye, *Carbohydr. Polym.*, 2018, **181**, 200.

79 N. Du, L. Y. Huang, Y. S. Xiong, R. Tian, J. Y. Yin and D. Y. Cao, *et al.*, Micro-mechanism insights into the adsorption of anionic dyes using quaternary ammonium-functionalised chitosan aerogels, *Carbohydr. Polym.*, 2023, **313**, 120855.

80 S. He, J. Li, X. Cao, F. Xie, H. Yang and C. Wang, *et al.*, Regenerated cellulose/chitosan composite aerogel with highly efficient adsorption for anionic dyes, *Int. J. Biol. Macromol.*, 2023, **244**, 125067.

81 Z. L. Yaneva and N. V. Georgieva, Insights into Congo Red Adsorption on Agro-Industrial Materials - Spectral, Equilibrium, Kinetic, Thermodynamic, Dynamic and Desorption Studies, *Review*, 2012, **4**, 127.

82 M. M. Abou Alsoaud, M. A. Taher, A. M. Hamed, M. S. Elnouby and A. M. Omer, Reusable kaolin impregnated aminated chitosan composite beads for efficient removal of Congo red dye: isotherms, kinetics and thermodynamics studies, *Sci. Rep.*, 2022, **12**(1), 1–19.

83 L. Liu, Z. Y. Gao, X. P. Su, X. Chen, L. Jiang and J. M. Yao, Adsorption removal of dyes from single and binary solutions using a cellulose-based bioadsorbent, *ACS Sustainable Chem. Eng.*, 2015, **3**(3), 432.

84 S. Chatterjee, S. Chatterjee, B. P. Chatterjee and A. K. Guha, Adsorptive removal of congo red, a carcinogenic textile dye by chitosan hydrobeads: Binding mechanism, equilibrium and kinetics, *Colloids Surf., A*, 2007, **299**(1), 146.

85 H. Y. Zhu, Y. Q. Fu, R. Jiang, J. H. Jiang, L. Xiao and G. M. Zeng, *et al.*, Adsorption removal of congo red onto magnetic cellulose/Fe3O4/activated carbon composite: Equilibrium, kinetic and thermodynamic studies, *Chem. Eng. J.*, 2011, **173**(2), 494–502.

86 X. Huang, P. Hadi, R. Joshi, A. G. Alhamzani and B. S. Hsiao, A Comparative Study of Mechanism and Performance of Anionic and Cationic Dialdehyde Nanocelluloses for Dye Adsorption and Separation, *ACS Omega*, 2023, **8**(9), 8634.

87 Li. Y. XinxinYang, H. Gao, C. Wang, X. Zhang and H. Zhou, One-step fabrication of chitosan-Fe(OH)3 beads for efficient adsorption of anionic dyes, *Int. J. Biol. Macromol.*, 2018, **117**, 30–41.

88 I. Langmuir, The adsorption of gases on plane surfaces of glass, mica and platinum, *J. Am. Chem. Soc.*, 1918, **40**(9), 1361.

89 H. Freundlich, Über die adsorption in lösungen, *Z. Phys. Chem.*, 1907, **57**(1), 385–470.

90 K. Vijayaraghavan, T. V. N. Padmesh, K. Palanivelu and M. Velan, Biosorption of nickel (II) ions onto Sargassum wightii: application of two-parameter and three-parameter isotherm models, *J. Hazard. Mater.*, 2006, **133**(1–3), 304.

91 Y. S. Ho, Selection of optimum sorption isotherm, *Carbon*, 2004, **42**(10), 2115.

92 M. Brdar, M. Šćiban, A. Takači and T. Došenović, Comparison of two and three parameters adsorption isotherm for Cr(VI) onto Kraft lignin, *Chem. Eng. J.*, 2012, **183**, 108.

93 R. Sips, On the structure of a catalyst surface, *J. Chem. Phys.*, 1948, **16**(5), 490.

94 L. B. L. Lim, N. Priyantha, S. A. A. Latip and Y. Lu, Sequestration of toxic congo red dye through the utilization of red dragon fruit peel: Linear versus nonlinear regression analyses of isotherm and kinetics, *Desalin. Water Treat.*, 2021, **218**, 409.

95 M. Usman, A. Ahmed, B. Yu, S. Wang, Y. Shen and H. Cong, Simultaneous adsorption of heavy metals and organic dyes by β-Cyclodextrin-Chitosan based crosslinked adsorbent, *Carbohydr. Polym.*, 2021, **255**, 117486.

96 Y. Zeng, X. Liu, Y. Zhang, Y. Qin, X. Tang and W. Zhang, *et al.*, Excellent regeneration, easy separation and high capacity of 3D chitosan–melamine sponge composites for anionic dye removal, *New J. Chem.*, 2023, **13**, 6342.

97 S. Chatterjee, M. W. Lee and S. H. Wooa, Adsorption of congo red by chitosan hydrogel beads impregnated with carbon nanotubes, *Bioresour. Technol.*, 2010, **101**(6), 1800.

98 S. Chatterjee, H. N. Tran, O. B. Godfred and S. H. Woo, Supersorption Capacity of Anionic Dye by Newer Chitosan Hydrogel Capsules via Green Surfactant Exchange Method, *ACS Sustainable Chem. Eng.*, 2018, **6**(3), 3604.

99 U. J. Kim, S. Kimura and M. Wada, Highly enhanced adsorption of Congo red onto dialdehyde cellulose-crosslinked cellulose-chitosan foam, *Carbohydr. Polym.*, 2019, **214**, 294–302.

100 Y. S. Ho and G. McKay, Pseudo-second order model for sorption processes, *Process Biochem.*, 1999, **34**(5), 451.

101 K. Y. Chong, C. H. Chia, S. Zakaria, M. S. Sajab, S. W. Chook and P. S. Khiew, CaCO3-decorated cellulose aerogel for removal of Congo Red from aqueous solution, *Cellulose*, 2015, **22**(4), 2683.

102 W. J. Weber Jr and J. C. Morris, Kinetics of adsorption on carbon from solution, *J. Sanit. Eng. Div.*, 1963, **89**(2), 31–59.

103 P. Wang, T. Yan and L. Wang, Removal of Congo Red from Aqueous Solution Using Magnetic Chitosan Composite Microparticles, *BioResources*, 2013, **8**(4), 6026.

104 Li. Y. XinxinYang, H. Gao, C. Wang, X. Zhang and H. Zhou, One-step fabrication of chitosan-Fe(OH)3 beads for efficient adsorption of anionic dyes, *Int. J. Biol. Macromol.*, 2018, **117**, 30–41.

105 S. Chatterjee, M. W. Lee and S. H. Wooa, Adsorption of congo red by chitosan hydrogel beads impregnated with carbon nanotubes, *Bioresour. Technol.*, 2010, **101**(6), 1800.

106 Z. Jing, Y. Li, Y. Zhang, K. Chen, Y. Sun and M. Wang, *et al.*, Simple synthesis of chitosan/alginate/graphene oxide/UiO-67 amphoteric aerogels: Characterization, adsorption mechanism and application for removal of cationic and anionic dyes from complex dye media, *Int. J. Biol. Macromol.*, 2023, **242**(P1), 124683.

107 C. Tang, P. Brodie, Y. Li, N. J. Grishkewich, M. Brunsting and K. C. Tam, Shape recoverable and mechanically robust cellulose aerogel beads for efficient removal of copper ions, *Chem. Eng. J.*, 2020, **392**, 124821.

108 C. Gerente, V. K. C. Lee, P. L. Cloirec and G. McKay, Application of Chitosan for the Removal of Metals From Wastewaters by Adsorption—Mechanisms and Models Review, *Crit. Rev. Environ. Sci. Technol.*, 2007, **37**(1), 41–127.

109 L. Wang and A. Wang, Adsorption properties of Congo Red from aqueous solution onto surfactant-modified montmorillonite, *J. Hazard. Mater.*, 2008, **160**(1), 173.

110 L. Zhang, P. Hu, J. Wang, Q. Liu and R. Huang, Adsorption of methyl orange (MO) by Zr (IV)-immobilized cross-linked chitosan/bentonite composite, *Int. J. Biol. Macromol.*, 2015, **81**, 818.

111 K. Litefti, M. S. Freire, M. Stitou and J. González-Álvarez, Adsorption of an anionic dye (Congo red) from aqueous solutions by pine bark, *Sci. Rep.*, 2019, **9**(1), 1–11.

112 S. Das, M. K. Kumawat, S. Ranganathan, R. Kumar, J. Adamcik and P. Kadu, *et al.*, Cell Alignment on Graphene – Amyloid Composites, *Adv. Mater. Interfaces*, 2018, **5**(18), 1800621.

113 K. Fan, T. Zhang, S. Xiao, H. He, J. Yang and Z. Qin, Preparation and adsorption performance of functionalization cellulose-based composite aerogel, *Int. J. Biol. Macromol.*, 2022, **211**, 1–14.

114 A. Munir, T. Haq, A. Qurashi, H. Rehman and A. Ul-hamid, Ultrasmall Ni/NiO Nanoclusters on Thiol Functionalized and Exfoliated Ultrasmall Ni/NiO Nanoclusters on Thiol-Functionalized and -Exfoliated Graphene Oxide

Nanosheets for Durable Oxygen Evolution Reaction, *ACS Appl. Energy Mater.*, 2019, **2**(1), 363–371.

115 F. Yang, Z. Yan, J. Zhao, S. Miao, D. Wang and P. Yang, Rapid capture of trace precious metals by amyloid- like protein membrane with high adsorption capacity and selectivity, *J. Mater. Chem. A*, 2020, **8**(6), 3438.

116 M. Mahapatra, M. Karmakar, A. Dutta, H. Mondal, J. Sankar and D. Roy, Journal of Environmental Chemical Engineering Microstructural analyses of loaded and/or unloaded semisynthetic porous material for understanding of superadsorption and optimization by response surface methodology, *J. Environ. Chem. Eng.*, 2018, **6**(1), 289–310.

117 M. Tan, S. Zheng, H. Lv, B. Wang, Q. Zhao and B. Zhao, Rational design and synthesis of chitosan-quinoa polysaccharide composite aerogel and its adsorption properties for Congo red and methylene blue, *New J. Chem.*, 2021, **45**(22), 9829.

118 P. Joshi, A. Raturi, M. Srivastava and O. P. Khatri, Graphene oxide, kaolinite clay and PVA-derived nanocomposite aerogel as a regenerative adsorbent for wastewater treatment applications, *J. Environ. Chem. Eng.*, 2022, **10**(6), 108597.

119 J. S. Stevens, A. C. De Luca, M. Pelendritis, G. Terenghi, S. Downes and S. L. M. Schroeder, Quantitative analysis of complex amino acids and RGD peptides by X-ray photoelectron spectroscopy (XPS), *Surf. Interface Anal.*, 2013, **45**(8), 1238.

120 S. S. S. Wang, P. L. Hsieh, P. S. Chen, Y. T. Chen and J. S. Jan, Genipin-cross-linked poly(l-lysine)-based hydrogels: Synthesis, characterization, and drug encapsulation, *Colloids Surf., B*, 2013, **111**, 423.

121 M. Peydayesh, S. Bolisetty, T. Mohammadi and R. Mezzenga, Assessing the Binding Performance of Amyloid – Carbon Membranes, *Langmuir*, 2019, **35**(11), 4161–4170.

122 F. Yang, Z. Yan, J. Zhao, S. Miao, D. Wang and P. Yang, Rapid capture of trace precious metals by amyloid-like protein membrane with high adsorption capacity and selectivity, *J. Mater. Chem. A*, 2020, **8**(6), 3438.

123 X. Zheng, X. Li, J. Li, L. Wang, W. Jin and J. Liu, *et al.*, Efficient removal of anionic dye (Congo red) by dialdehyde microfibrillated cellulose/chitosan composite film with significantly improved stability in dye solution, *Int. J. Biol. Macromol.*, 2018, **107**, 283.

124 Z. Jing, Y. Li, Y. Zhang, M. Wang, B. Chen and Y. Sun, *et al.*, Effective Removal of Congo Red from Water using Chitosan@UiO-67 Hydrogel Spheres: Synthesis, Characterization and Adsorption Mechanisms, *ChemistrySelect*, 2023, **8**(20), 202204367.

125 K. L. Hudson, G. J. Bartlett, R. C. Diehl, J. Agirre, T. Gallagher and L. L. Kiessling, *et al.*, Carbohydrate-Aromatic Interactions in Proteins, *J. Am. Chem. Soc.*, 2015, **137**(48), 15152.